

TOPICAL REVIEW • OPEN ACCESS

## Towards *in-situ* quality control of conductive printable electronics: a review of possible pathways

To cite this article: Mariia Zhuldybina *et al* 2021 *Flex. Print. Electron.* **6** 043007

View the [article online](#) for updates and enhancements.

You may also like

- [Simulation of the Piezoelectric Effect on the Device Characteristics of AlGaIn/GaN Insulated-Gate Heterostructure Field Effect Transistors](#)  
Syunji Imanaga and Hiroji Kawai
- [Interfacial Process for Electrochemical System Using Polyelectrolyte Membranes for High-Performance Electroplating](#)  
Kensuke Akamatsu, Ryosuke Fujiwara, Yohei Takashima *et al.*
- [Effects of interface on electrical conduction in polyethylene-\(ethylene-vinyl acetate\) copolymer composites](#)  
Y Suzuki, G Cai and M Ieda



The Electrochemical Society  
Advancing solid state & electrochemical science & technology

242nd ECS Meeting

Oct 9 – 13, 2022 • Atlanta, GA, US

Abstract submission deadline: **April 8, 2022**

Connect. Engage. Champion. Empower. Accelerate.

**MOVE SCIENCE FORWARD**



Submit your abstract



# Flexible and Printed Electronics



## TOPICAL REVIEW

### OPEN ACCESS

RECEIVED  
27 October 2021

REVISED  
12 December 2021

ACCEPTED FOR PUBLICATION  
17 December 2021

PUBLISHED  
31 December 2021

Original Content from  
this work may be used  
under the terms of the  
[Creative Commons  
Attribution 4.0 licence](#).

Any further distribution  
of this work must  
maintain attribution to  
the author(s) and the title  
of the work, journal  
citation and DOI.



## Towards *in-situ* quality control of conductive printable electronics: a review of possible pathways

Mariia Zhuldybina<sup>1,2</sup>, Xavier Ropagnol<sup>1,3</sup> and François Blanchard<sup>1,\*</sup>

<sup>1</sup> Département de Génie Électrique, École de Technologie Supérieure (ÉTS), Montréal, QC H3C1K3, Canada

<sup>2</sup> Institut des Communications Graphiques et de l'imprimabilité, Montréal, QC H2M2E2, Canada

<sup>3</sup> Institut National de la Recherche Scientifique, Énergie, Matériaux et Télécommunications (INRS-EMT), Varennes, QC J3X1S2, Canada

\* Author to whom any correspondence should be addressed.

E-mail: [francois.blanchard@etsmtl.ca](mailto:francois.blanchard@etsmtl.ca)

**Keywords:** flexible and printed electronics, roll-to-roll printing, non-destructive testing, terahertz, infrared, smart manufacturing

### Abstract

Over the past decade, printed electronics (PE) has shown great potential for a wide range of industries, from consumer goods, electronics, aerospace, automotive, pharmaceutical, biomedical, to textiles and fashion. The rapid development of printing technology has been strongly driven by the growth of the PE market and its many applications. Here, we review the latest trends in PE production quality control, focusing on emerging technologies such as terahertz spectroscopy, which may play a key role in the development of smart manufacturing of PE devices in the near future. We also provide a comparison with conventional quality control technologies or off-line measurements, such as four-point probe measurements, atomic force microscopy, optical microscopy, etc.

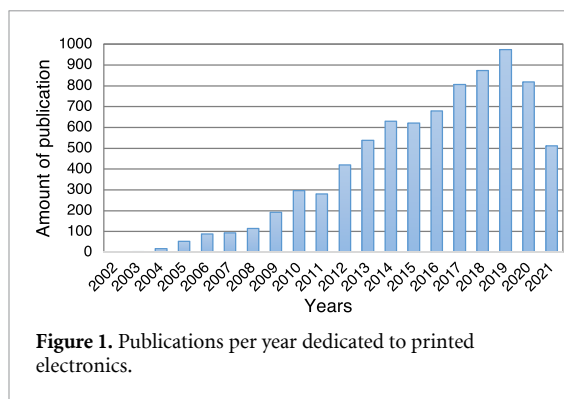
## 1. Introduction

Today, modern industry is increasingly adopting an information system known as the Internet of Things (IoT) [1], in which permanently integrated smart devices and sensors collect and exchange data. The fabrication of low-cost devices is one of the main research interests in this field, where new manufacturing techniques, such as printed electronics (PE), offer an attractive solution for the device component of IoT. This manufacturing technology enables the printing of a wide range of low-cost customized electronic devices ranging from sensors and packaging, and going all the way to smart clothing [2].

PE is an advanced manufacturing technology that enables large volume production of electronic devices. It provides an attractive alternative to conventional circuit manufacturing by enabling simple, maskless, rapid and low-cost production [3]. The development of PE originated from organic electronics, whose story dates back to 1977 with the efforts of Shirakawa *et al* [4]. They discovered that polymer could be conductive by doping certain molecules, and their discovery earned them the 2000 Nobel Prize in Chemistry. The development of printing technology has been fastened by the rapidly growing PE market

and by its numerous applications. Keslinen *et al* [5] predicted the rapid growth of the PE market, with projected total revenues of \$2.2 billion in 2011, and expected to reach \$73.3 billion by 2029 [2, 5]. Since the first demonstration of printable transistors on polyester film by Bao *et al* [6], the fields of application of PE devices has grown steadily, with a concomitant increase in the total number of PE-related publications per year, as shown in figure 1.

Because PE production is fast-paced, quality can vary considerably throughout the printing process. This process can be divided into three main parts: (a) ink and substrate selection, (b) actual printing, and (c) sintering. The production begins with an ink and a substrate. While PE is compatible with a wide range of substrates, it is flexible substrates, however, that attract the most attention as they provide additional modalities such as bendability, stretchability, and twistability, while maintaining their electrical properties [7]. Furthermore, various types of conductive, semi-conductive and dielectric inks are now commercially available for different types of printing [8]. The ink type is chosen based on the future printing process and device applications. In addition, the formulation of inks from compostable and recyclable materials is the subject of intensive research [9]. To



date, area that has attracted the most interest in PE is conductive ink [10].

Once the substrate and ink are chosen, the next step is to print the device. Various contact and non-contact printing technologies exist, such as flexography, gravure, screen, and inkjet printing [11]. All these methods have been significantly adapted from printing on paper to the needs of PE. The final, but not the least significant, step is the drying or sintering of the ink. This process is highly dependent on the properties of the ink and plays an essential role in lending the ink its functionalities, e.g. conductivity, semiconductivity and dielectricity, which allows to obtain a pattern from a printed design [12]. The most commonly used sintering methods are conventional thermal annealing, electrical sintering, microwave sintering, and photonic sintering by continuous wave laser irradiation or high-power flash lamp [10].

Throughout the printing process, quality control (QC) must be evaluated, and this continues to be a challenge. At this point, it is interesting to draw a parallel with the inspection methods in the well-established graphic printing industry. Obviously, the main parameters to control for graphic printing are different, and consist mainly of colour, resolution, register and surface finishes [13]. In graphic printing, the devices to be printed have no functionality, and QC is evaluated only for the printing process. In contrast, the PE manufacturing process is responsible for printing functional devices, which means that QC must be evaluated for the printing process itself and the device functionality.

This review is dedicated to summarizing the current state of the art practices for QC in conductive PE. It is organized as follows: in section 2, we summarize information on existing QC tools for PE production and manufacturing. We detail various practical implementations of these tools. Section 3 is dedicated to the quality control assessed for the graphic printing industry, which can be the leading strategy for the quality control in the PE industry. In section 4, we divide the type of QC for classical and emerging techniques. This information is also categorized for production steps. This review can be

used for scientific and commercial interests to guide towards the best choice for a QC that will improve the reproducibility and reliability of PE production. Particular attention is devoted to future avenues that will enable *in-situ* process monitoring in an industrial production environment. This path is important as it will enable closed-loop quality control to ultimately achieve intelligent PE manufacturing.

## 2. Production of printable electronics

To better understand the challenges in characterizing the production of PE devices, it is worth reviewing the different printing methods and their particularities. To this end, the following section presents a detailed discussion of the characteristics of the inks used to produce PE devices, the printing methods, and the various sintering procedures.

### 2.1. Inks and substrates

Nowadays, different types of conductive, semiconductive and dielectric inks are commercially available [10, 14, 15], and a specific ink functionality is developed for each PE component. A typical ink is formulated from resins, vehicles, additives, and active materials [9–11]. The resins have the most significant influence on the properties of the ink and determine the bonding of the formulation ingredients to each other, as well as adhesion to the substrate [11]. The liquid part of the formulation is a vehicle responsible for transferring the ink to the substrate and defining the drying rate. Additives improve the properties of the functional materials or provide additional properties. The active material is responsible for the target functionality of a dried film. The main criteria for the selection of the active material(s) are the energy required for drying and obtaining the desired performance value and the physicochemical characteristics of the material(s). These include material geometry considerations: 3D dimensions, the size distribution, and modifications to facilitate the ink formulation steps [9–11]. Different proportions of the ink's constituents determine the ink characteristics: rheology, viscosity, surface tension, oxidation, etc [9]. Ink development is in high demand, especially as existing electronics devices are being transitioned to eco-friendly, bio-sourced, and biodegradable PE devices in a bid to alleviate the environmental footprint of standard electronics [16–18].

The manufacturing of printable electronic components begins with the printing of conductive layers and is then completed by layers of semiconductors or dielectrics. Most conductive inks are made from metallic nanoparticles (NPs) [10]. Typically, they consist of suspensions of metallic NPs in liquid. Each NP is encapsulated in a layer of insulating organic additives and stabilizing agents to prevent its agglomeration as well as current flow between particles.

**Table 1.** A comparison between printing methods.

Type of printing	Flexography	Gravure	Screen-printing	Inkjet
Ink viscosity (Pa·s)	0.01–0.1	0.01–0.4	0.1–10	0.001–0.04
Printing form	Relief	Engraved cylinder	Stencil/screen	N/A
Image transfer	Direct	Direct	Direct	Non-contact
Line width ( $\mu\text{m}$ )	5–50	5–25	30–50	1–20
Film thickness ( $\mu\text{m}$ )	0.25–4	0.25–6	0.5–200	0.15–15
Printing speed ( $\text{m min}^{-1}$ )	5–180	2–100	0.6–100	0.02–5
Common defects	Halo around patterns; marbling	Irregular edges around printed dots	Irregular edges and lines	Coffee ring

Organic additives and solvents are evaporated during a post-printing step [19].

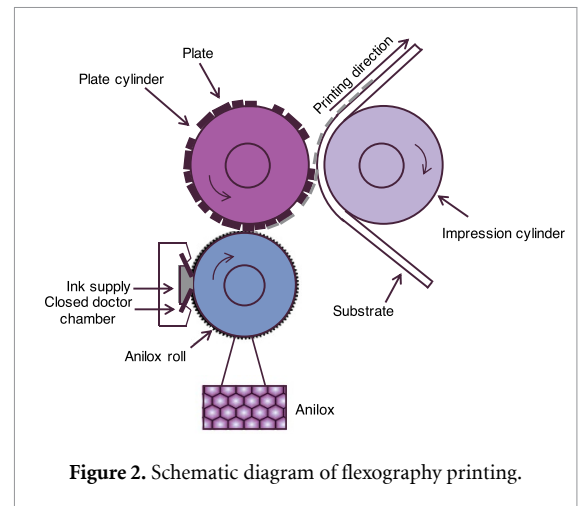
Some PE printing technologies allow the use of traditional rigid substrates such as silicon or glass [5, 20]. However, one of the main interests for PE is the design on flexible substrates. Compared to conventional methods, the low processing temperature under which PE proceeds makes the technology compatible with most inexpensive plastic films, which are generally nonporous and can withstand all manufacturing steps, including pre- and post-printing processes [21]. The most commonly used flexible substrates are polyimide (PI), polyethylene terephthalate (PET), and polyethylene naphthalene (PEN) sheets [5].

## 2.2. Printing techniques

Printing techniques used in the graphic printing industry have been developed for decades. During the last decade, most standard printing methods have been adapted to meet the needs of printed electronics. The printing step consists in depositing materials on the substrate with the required resolution and definition. In this review, we limit ourselves to an examination of the printing capabilities of the methods suitable for roll-to-roll (R2R) printing [2, 7, 11, 22–25], which includes the operating principle of flexographic, gravure, screen and inkjet printings. We pay particular attention to the parameters that can affect the printing quality. Table 1 summarizes the main characteristics of each printing technique and its typical defects [11, 25].

### 2.2.1. Flexography printing

Flexographic printing is a high-speed, continuous R2R process, which is a well-known manufacturing technique commonly used by the packaging, label and newspaper industries [26]. The minimum printable element size is about  $50 \mu\text{m}$  and its exceptionally high throughput (up to  $35 \text{ m}^2 \text{ s}^{-1}$ ) significantly reduces production costs [7, 26, 27]. Figure 2 illustrates the basic principle of flexographic printing. In a first step, the ink is put in contact with a micro-engraved cylinder (anilox) and fills its cells. The cylinder is then scraped with a doctor blade to ensure that the cells are filled with a constant and controlled volume of ink [13]. Aniloxes are defined by their theoretical volume,

**Figure 2.** Schematic diagram of flexography printing.

and in North America, this volume is expressed as  $10^9 \mu\text{m}^3$  of ink contained in  $1 \text{ in}^2$  of cells or billion cubic microns per square inch, typically written as  $\text{bcm} (\text{in})^{-2}$ ,  $\text{bcm} (\text{sq-in})^{-1}$ , or  $\text{bcm}$  [11]. Correctly choosing the anilox may help obtain the proper ink distribution during the process.

In a second step, the ink is transferred onto a cylindrical printing plate made of rubber or to a photopolymer. The printing form defines the pattern information engraved as a positive relief in the printing plate soft structure. Afterward, the inked pattern is pressed against the substrate in the nip zone between the printing form and an impression cylinder. The ink transfer onto the substrate is performed with the lowest possible pressure. This particularity has given led to flexography receiving the nickname ‘kiss printing’. Due to the low pressure applied in the nip, the flexography process is able to transfer ink onto a wide range of substrates, varying from fragile substrates such as corrugated boards, which can be flattened during printing, and self-adhesive labels that contain a layer made of adhesive, to smooth substrates such as plastics, foils and glass. The thickness of the printed film is defined by the anilox parameters, as well as by the transfer rates from the printing plate cylinder to the printing substrate. A halo around patterns and marbling are the most common defects appearing during this process [11]. In-line quality control can lead to immediate process optimization, i.e. through changes in pressure between the printing

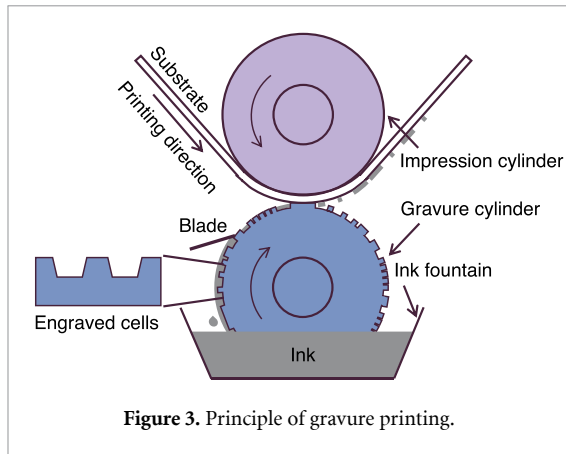


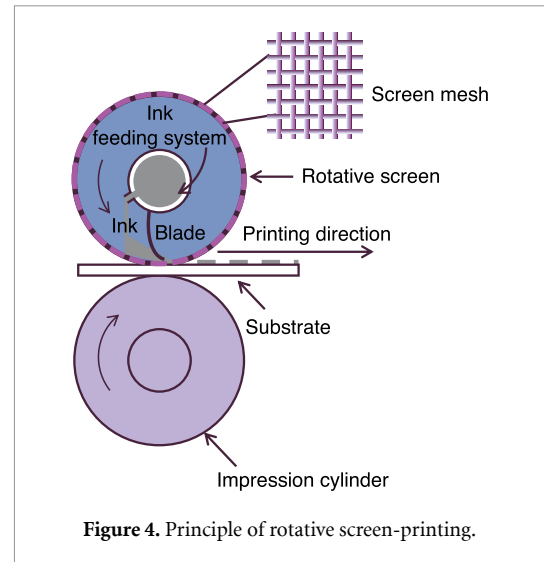
plate cylinder and the printing substrate, thus avoiding defects related to ink distribution.

### 2.2.2. Gravure

Gravure or rotogravure printing is described in figure 3. This printing process produces higher quality results as compared to the other printing methods, and is used to produce periodicals, magazines, and catalogs. It is a rotary process based on the use of a cylinder that engraves the design into the surface. The design is split into printing areas, namely, engraved cells, non-printed areas, and cell walls. Depending on the engraving technology used, the cells have a variable depth and/or variable area. This depth and area define the potential quantity of ink which may be transferred onto the substrate. As a first step, the cells are filled with ink from a reservoir in which the gravure cylinder is rotating. The doctor blade scrapes the cylinder to remove excess ink from the non-printed area and controls the volume of ink in the cells. Then, the ink is put in contact with the substrate in a nip zone located between the printing form and a printing cylinder. The most common printed defect is irregular edges around printed dots. However, this defect can be corrected by engraving techniques during the pre-printing step [11].

### 2.2.3. Screen-printing

Another common technique is screen printing, which has long been actively used for the production of textiles, automobile dashboards, and printed circuit boards. It involves forcing a pasty ink to go through the openings of a meshed screen with a squeegee. The mesh is covered by a stencil that blocks the non-printed area. Rotary screen printing uses a printing screen, which is rolled to form a hollow cylinder with the blade and the inking system lodged in its cavity. The cylinder turns in synchronization with the substrate, and, in the nip zone, the static blade forces the ink to transfer from the mesh to the substrate, as described in figure 4. The mesh counts can be varied from 40 to 230. A higher mesh counts provides finer details, but this could be problematic for nanoparticle-based inks. One of the advantages



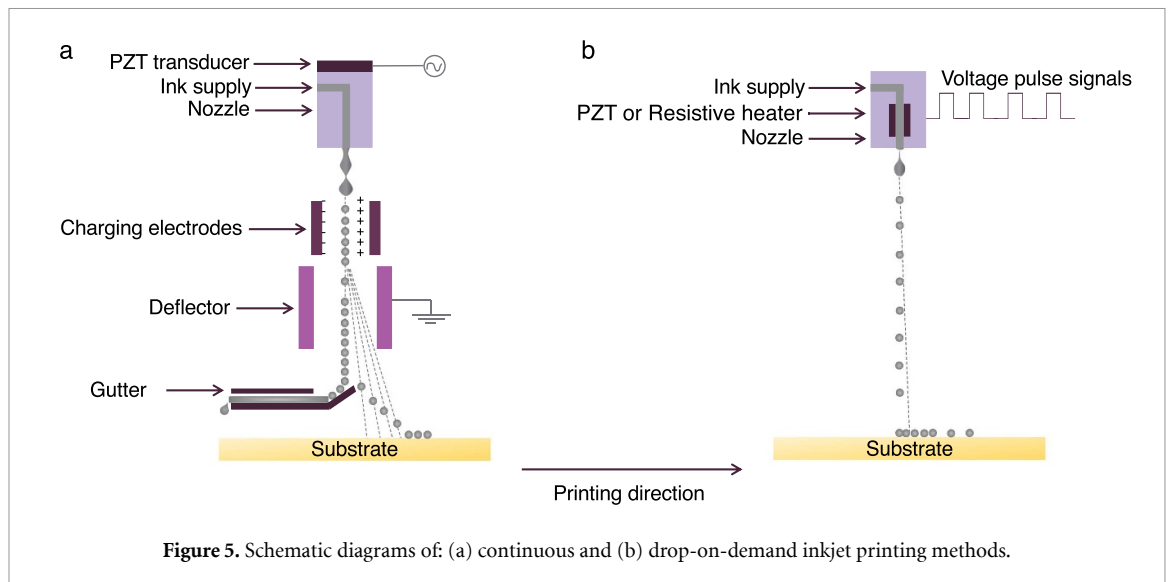
of this method is that it produces a high ink thickness, but with low definition caused by irregular edges and lines. In the pre-printing stage, this problem can be controlled or eliminated by properly aligning the mesh lines and wires. For an in-line solution, blade pressure sensing could provide direct feedback to facilitate any necessary adjustment.

### 2.2.4. Inkjet-printing

The benefits of inkjet printing include low production cost, contactless deposition, and high resolution for printing fine features onto various substrates [11, 28, 29]. The printer is controlled directly by an image processor in digital format, and can easily change and adjust the printing pattern. This printing technique opens the possibility for a new way to produce printed media, e.g. print-on-demand, personalized devices, and home printing [25]. The major disadvantage with inkjet printing is cartridge printhead clogging. To circumvent this, dedicated printing protocols must be developed for different types of ink, which leads to enormous material waste [11, 30]. All inkjet printing techniques are based on the digitally controlled ejection of drops of fluid from a print head. Figures 5(a) and (b) show schematic diagrams of the two typical inkjet printing techniques: continuous (CIJ) and drop-on-demand (DOD), respectively.

A CIJ printer operates by channeling a continuous stream of ink through a nozzle. It uses plate electrodes to selectively charge individual droplets in a falling jet. The charged droplets are then directed to the proper location on the substrate by an electric field, while uncharged droplets are collected and returned for reuse.

Thermal DOD inkjet is the technology most used in desktop printers. In this technology, the print cartridges consist of series of tiny chambers, each containing a heater. A pulse of current is passed through the heating element, causing the rapid formation of



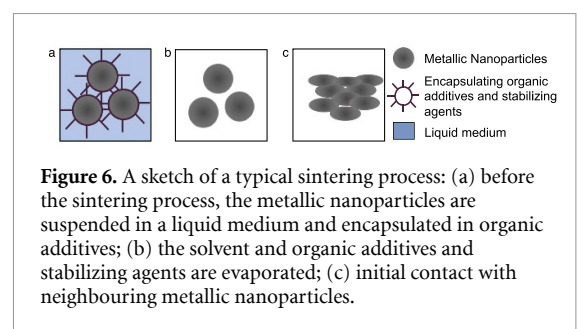
gas bubbles, which forces ink to leave the nozzle due to an increase in pressure. The ejected drop leaves a void in the chamber that is subsequently filled by a replacement fluid in preparation for creating the next drop [2]. Meanwhile, most commercial and industrial inkjet printers use the mechanical deformation of piezoelectric materials for the ejection of ink droplets. The voltage signal is applied to a piezoelectric transducer to control the ink droplet volume and velocity, as well as the ink frequency. Drop formation in piezoelectric DOD printing systems highly depends on the ink properties and input electric voltage waveforms for a given piezoelectric material and nozzle characteristics [2, 9, 11, 31].

### 2.3. Drying/sintering

Once the ink is printed onto a substrate, post-press processes are then needed to realize the manufacture of PE devices [32, 33]. The most commonly used drying/sintering approaches are conventional thermal annealing [10, 34, 35], microwave sintering [36, 37], and photonic sintering by either continuous-wave laser irradiations [14, 38] or high-power flashing lamps [12, 39]. Solid and uniform dielectric or metallic tracks from the printed pattern are obtained during this step. The electrical properties of printed patterns depend entirely on this process. This is also the reason why this processing step may be the most favorable for the inclusion of an in-line characterization method [40].

#### 2.3.1. Thermal treatment

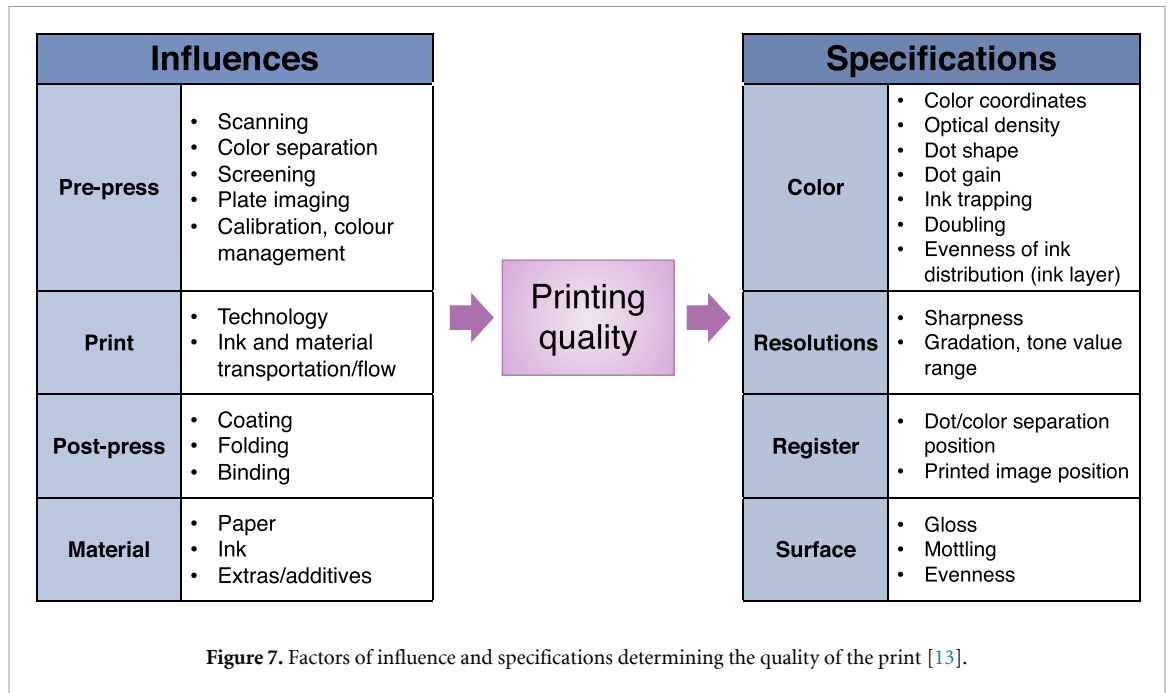
The standard method to convert printed non-conductive inks to conductive counterparts involves heating by drying in a chamber, using a hot plate, or in a convection oven [34, 35]. During the printing process, the substrate is slightly heated at a relatively low temperature ( $\sim 60$  °C) to initiate the adhesion of ink with the substrate. As shown in figure 6(a),



at this point, the conductivity of the printed patterns is very low because the metal nanoparticles are still separated by solvent and encapsulated in organic additives and stabilizing agents. When sintering is started, the liquid is evaporated, and its volume is equal to the decrease in volume of the particle network [7, 41]. Once all organic components are melted, nanoparticles are arranged tidily in a single layer film as depicted in figure 6(b). Necks begin to grow between contacting nanoparticles, leading to the growth of grains [42]. Figure 6(c) indicates the increase in density from the time the particle became compact. Further, the pores around the grains begin to collapse, and the film densification is at a maximum. The increase in the sintering temperature leads to the growth of the grains, the boundaries recede, and the pores are completely collapsed. Since the sintered ink structures contain some defects (for example, an incomplete contact between particles and residual porosity), the resulting conductivity is lower than that of bulk material. One disadvantage of this technique is that it trades off the ink stability, which may affect printing repeatability and long-term storage [35].

#### 2.3.2. Photonics sintering

Traditional thermal baking is the most used method for sintering or drying printed traces. However,



achieving a proper functionality of printed devices requires sintering over a long period. Furthermore, this type of sintering is not compatible with the thermal stability of commonly used inexpensive polymer foils (e.g. PET or PEN) [43, 44].

Photonic sintering has certain advantages over traditional thermal baking. It uses intense pulsed light to selectively sinter metal NP inks, reducing the heat-affected zone, and is especially relevant for plastic electronics applications. Dark-coloured printed NP inks have a higher absorbance capacity of the radiant energy of the lamp than the polymer substrate, which results in a faster increase in temperature in ink and causes rapid sintering of the metal nanoparticles, without affecting the substrate [39, 45]. These advantages increase the manufacturing throughput, reducing the post-fabricating process to a few seconds. The photonic sintering mechanism of metal NPs is similar to that of thermal sintering. However, during the photonic sintering, light absorbed by the printed metallic layer results in its heating, followed by liquid evaporation and sintering.

### 3. A glimpse into the characterization of graphic printing

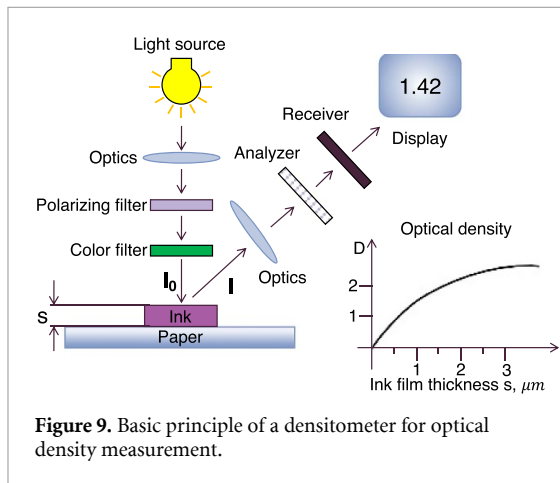
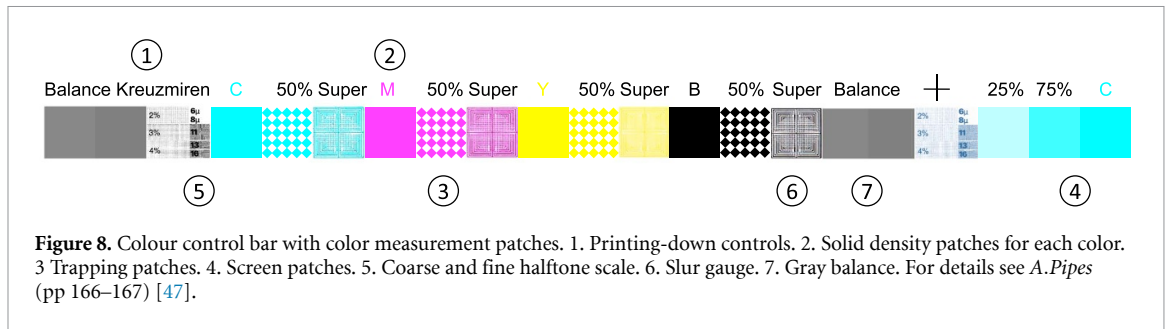
Before reviewing PE characterization methods, we thought a digression toward a characterization of graphic printing might help readers see how a similar industrial manufacture has managed certain aspects of its production quality. As mentioned earlier, only the printing process is assessed in graphic printing because no functionality can be expected from this manufacturing. Graphic printing products include newspapers, magazines, packaging, and many other

products, in which image rendering is the key parameter to control.

In this industry, various QC methods have been implemented to ensure the quality of the printing process. For example, for colour inks, QC monitoring can be done with in-line colour measurement based on colorimetry, transmission and reflectance spectroscopy [13, 46]. The parameters to be recovered depend on the type of printing (monochrome or multicolour) and the nature of the printing (an image or text). Information about the reproduction of fine structures, the range of tonal values, the accuracy of multicolour overprinting and the surface properties of the printed image are monitored in the quality control process. Figure 7 combines the factors that define the print quality according to the parameters that influence the printing process [13].

Retrieving such information on a large-scale manufacturing process and in real time is an extreme challenge, and likely not feasible. To solve this problem, the graphic printing industry uses a colour control bar that is usually printed away from the main product, for example, on the edge. The idea is to have a quality mark at a given time, proportional to the overall condition of the print. Figure 8 shows a typical colour control bar with colour measurement patches [47]. The colour control bar consists of the information required to know its quality, and can include solid tones (2), halftones (5), gray balance (7), and trapping patches to control solid colour overprint (3) [47].

Colorimetry was developed for use in the graphics industry as a means of quality testing printed media, with a requirement to detect small changes in printed colour. It allows to measure the chromatic stimulus, from which the colour stimulus specification

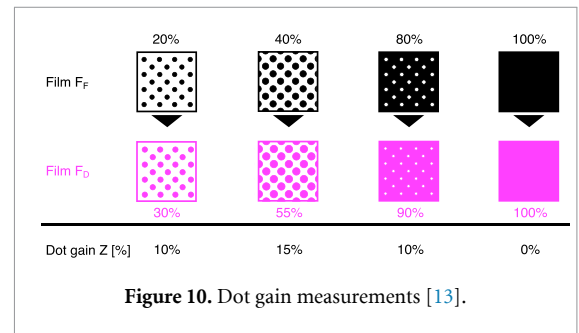


and colour perception can be deduced numerically by means of suitable interpretation models for standard colour spaces defined by the CIE: CIELAB, and CIELUV. The different models represent the spectral distribution of colours in a particular order [13, 46]. Colorimetry is based on techniques in which colours are measured as they are perceived by the human eye. Another technique used to measure colour variation is densitometry, which measures an ink film thickness that has been adapted to the inks used in the print, and in which the processing of measurement values is also adapted to human perception/sensitivity in relation to changes in lightness/saturation. Figure 9 shows an example of densitometric measurements performed to extract the optical density ( $D$ ) in the form of the logarithmic ratio [13]:

$$D = \log \frac{I_0}{I} = \log \frac{1}{\beta}, \quad (1)$$

where  $I_0$  and  $I$  are the intensities of the incident and reflected light by the ink, respectively.  $\beta$  is a reflectance factor equal to the ratio between the light intensities.

The reflectance factor depends on the thickness, and therefore, the reciprocal value  $1/\beta$  is established first. Then, the logarithm of  $1/\beta$  is related to the non-linear human visual perception. Typically, the densitometer is calibrated to the substrate with a '0' value. Different colours are measured with the same light source by inserting the colour filters in the path of the light beam. Part of the control bar includes a test



area for each colour in the cyan, magenta, yellow, and black (CMYK) model (also called process colour or four-colour process), which refers to the four ink plates used in some colour printing.

The other critical factor in the transfer of the printed image is the variation in dot diameter, which may lead to tonal and colour shifts. The dot gain/tonal value ( $Z$ ) is obtained from the difference between the area covered by the designed pattern ( $F_F$ ) and the area of the transferred ink ( $F_D$ ) [13]:

$$Z = F_F - F_D. \quad (2)$$

Using the halftones bar (4) in figure 8, the dot gain is calculated (see figure 10). For example, the printed ink coverage area ( $F_D$ ) is 55%, while the halftone patch was designed for 40%, resulting in a dot gain of 15%. Typically, dots expand during printing, and to avoid this, design patterns are made with a pre-compensation in order to minimize the expansion (0%).

Reliable colour control with colour bars throughout the print run can only be assured by a densitometer or colorimeter that takes measurements on the press during printing. In addition, the inspection of the final printed image is a must. Typically, the visual inspection of the running press uses a periodic flash of light generated from a stroboscope, which is synchronized with the press speed. An optical system incorporates a rotating mirror to provide a high-quality image inspection. The static image quality allows the press operator to detect larger colour changes.

It is likely that how graphic printing is characterized can serve as a guide for future inspection methods in the mass production of PE devices.

**Table 2.** Abbreviation of characterization methods and their application during the printing process (blue cells).

	Technique	Abbreviation	Materials	Printing process	Sintering	Device properties
Classical	Atomic force microscope	AFM	■			
	Contact angle					
	Ellipsometry			■		
	Four-point probe	4PP			■	■
	Fourier-transform infrared	FTIR	■		■	
	Multimeter					■
	Nanoindentation				■	
	Optical microscopy	OM	■			
	Optical profilometry	OP		■		
	Raman spectroscopy		■		■	
	Scanning electron microscope	SEM	■			
	Stylus profilometry	SP		■		
	Ultraviolet-Visible-Near Infrared spectroscopy	UV-Vis-NIR	■			
Emerging	All-optical difference engine sensor	AODE		■	■	
	Frequency-domain thermoreflectance	FDTR		■	■	
	Eddy current testing	ECT		■	■	
	Light-emitting diodes-based optical inspection	LED		■	■	
	Non-linear optical microscope	Non-linear OM		■	■	
	Small angle x-ray scattering	SAXS		■	■	
	Synchronized thermography	ST		■	■	
	Terahertz time-domain spectroscopy	THz-TDS		■	■	

It is likely that the way to characterize graphic printing can serve as a guideline for future inspection methods for mass production of PE devices.

## 4. Characterization of the PE

When producing a PE device, the first control is a visual inspection to identify the geometry of the printed layers, the defects, and their sintering level. As mentioned previously, this last parameter is very important because it strongly affects the electrical functionality of the conductive ink. Unlike graphic printing, where the drying step is important for defining colour brightness, the parameters of the drying/sintering step are crucial for the future electrical functionality, which depends on: (a) the type of printed ink, (b) the sintering method, (c) the sintering time, and (d) the temperature, in the case of thermal sintering, or the laser power and speed, in the case of photonic sintering. In addition, the morphology of the printed lines and their mechanical and electrical properties are among the characteristics to be evaluated. This section describes the methods developed for *ex-situ* and *in-situ* QC measures for the PE production process and the functionality of printed devices.

To describe characterization techniques, we split them into two main categories: classical and emerging methods. The most common techniques that have come to our attention are listed in table 2. The highlighted areas show the printing step, where the method can be applied.

### 4.1. Classical methods

#### 4.1.1. Characterization of the preprint

Before printing on an industrial scale, the compatibility between the materials used must be tested. Typically, the contact angle between an ink and a substrate ( $\theta_{(\text{ink-sub})}$ ) shows the matching between their surface tension and surface energy, respectively. To extract this angle, the Young-Dupre equation is used [11]:

$$\gamma_{(\text{sub-air})} = \gamma_{(\text{ink-sub})} + \gamma_{(\text{ink-air})} \cos \theta_{(\text{ink-sub})}, \quad (3)$$

where  $\gamma_{(x-y)}$  is the surface tension between the air and the substrate (sub-air) or the ink (ink-air) or between the ink and substrate (ink-sub), respectively [30, 48].

To find out  $\gamma_{(\text{sub-air})}$ , the sessile drop method is usually applied, where liquids with a known surface energy are deposited onto the tested substrate [30]. Knowing the surface tensions of the substrate and of the ink, the contact angle ( $\theta_{(\text{ink-sub})}$ ) can be extracted, as shown by Nguyen *et al* [22]. The extracted value shows the ink wetting behaviour. The most ideal case is a contact angle close to  $90^\circ$ , which results in equilibrium conditions [11]. The ink wetting behaviour directly affects the widening of printed patterns during the process [22, 37].

The low surface energy of polymer substrates may cause the poor adhesion between an ink and a substrate. To overcome this problem, surface treatments are required to modify the surface energy of the polymer. Mostly corona discharge [49, 50], plasma and chemical treatments [51] are used. It gives a temporary effect, however, improves the compatibility of the surface with the ink by bring to an increase of

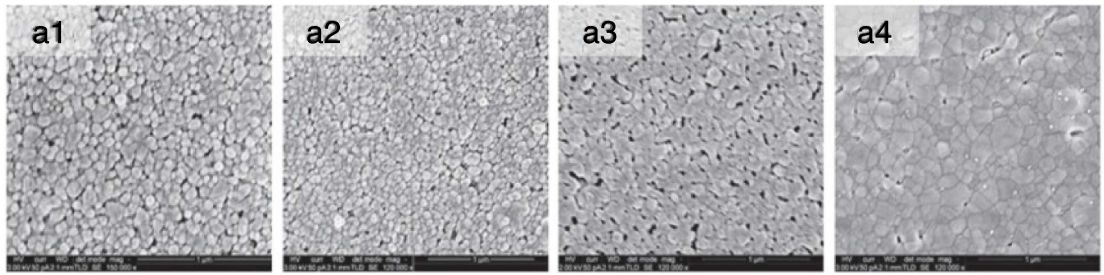


**Figure 11.** Laser sintering evolution as indicated by HR-SEM images taken at four different stages of the process for silver ink D50BA (supplied by PV Nanocell). Reprinted with permission from [12].

the surface energy of a solid surface. Hence, it exceeds the liquid surface tension and results in enhancing of adhesion between an ink and a substrate [51, 52].

Another factor that affects the printed pattern dimensions is the intrinsic conditions of the printing parameters, which could be theoretically pre-determined depending on the type of printing. For example, in gravure printing, the nip pressure is most dominant over the ink transfer ratio ( $\eta_T$ ) [22]. A mathematical model is used to estimate the width of printed patterns ( $w_p$ ) as a function of the contact angle and ink transfer ratio:

$$w_p = 2 \sin \theta_{\text{ink-sub}} \sqrt{\frac{\eta_T A_{\text{cell}}}{\theta_{\text{ink-sub}} - \sin \theta_{\text{ink-sub}} \cos \theta_{\text{ink-sub}}}} \quad (4)$$

where  $A_{\text{cell}}$  is the cell geometry of a gravure printing roll. For example, in the digital printing process, Sowade *et al* pre-calculated the number of printed pixels for different print directions to automatically reduce edge defects and widening [37].

Once suitable materials are found, the printability and the surface morphology must be evaluated. To this end, the arrangement of the molecules in the printed layer is characterized by powerful imaging techniques [53]. Scanning electron microscopy (SEM) and atomic force microscopy (AFM) are commonly used to investigate the printed surface morphology [40, 53]. The SEM forms a 2D image by a raster scan of the electron beam across the surface, recording the intensity value of emission from the sample at each  $(x, y)$  data point [54]. For example, SEM has been actively used to study the surface and the cross-section morphology of a printed layer made from a metallic nanoparticles ink for different sintering methods [12, 33, 43, 45, 55–62]. Figure 11 shows SEM images of progressive morphological changes due to applied photonic sintering with different exposure times [12]. In figure 11(a1), the printed ink is in the unsintered stage, where NPs are well separated. The following image (see figure 11(a2)) shows an early stage of the sintering process, where contacts between nanoparticles start to form since the organic material has been removed and resistivity reaches  $\sim \times 100$  of bulk silver. In figure 11(a3), we

can observe the neck formation, driven by the minimization of the surface energy. At this stage the resistivity is around  $\sim \times 10$  of bulk silver. The last stage of sintering shows that the individual nanoparticles turn into larger single crystal grains. These morphological changes lead to a significant improvement of the conductivity ( $\sim 30\%$  of bulk silver) [12, 33, 43, 45, 55–62].

In general, SEM provides information on sample topography, material chemistry, and surface morphology. In addition, SEM allows the study of crack formation and edge effects that result in cross-sectional variation and limited connectivity between solid particles [27]. It can easily be seen that the latter parameter is crucial for the PE device [21, 63].

Although SEM is a very important and well-established technique, it requires a vacuum environment for high quality imaging under optimal conditions, which slows down the results. In contrast, AFM can be used in the open air under ambient conditions. Unlike SEM, the data obtained provides information on the surface in 3D [54]. Typically, AFM captures the topography along with a phase image [64, 65]. Depending on the physical properties of a surface, i.e. stiffness, elasticity, and viscosity, the interaction between the tip and the surface will cause a phase shift. The phase image can reveal information that is hidden in the topography images [64, 65]. Figures 12(a) and (b) show the topography and (c), (d), the phase images. In the topography images of the printed PEDOT:PSS-Au ink, the bright areas are particles that protrude from the surface and have a higher intensity because they are the highest features. The rest of the surface is not very clear, even using higher magnification, as in figure 12(b). In contrast, figures 12(c) and (d), which are the phase images of the sample, clearly show the nanoparticles and connections between them [64]. The dark area corresponds to the lowest phase shift and represents the pores between the nanoparticles, which have a higher phase shift due to their properties.

SEM and AFM have the advantage of providing high resolution images of a few nm and allow the study of ink morphology [66–68]. However, they require specific conditions, such as vacuum or

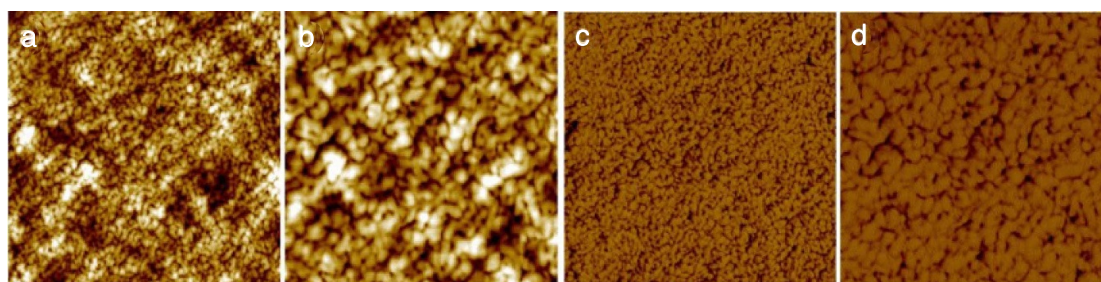


**Figure 12.** AFM topography images ((a) and (b)) and their respective phase contrast images ((c) and (d)) upon inkjet printing of the composite PEDOT:PSS-AuNP ink (scan size: (a) and (c))  $1\ \mu\text{m} \times 1\ \mu\text{m}$ . Reprinted with permission from [64].

helium environments, to avoid noise and damage [50, 53, 59, 69–73].

UV–Vis–NIR spectroscopy is another well-established technique that is used in a wide range of domains. Traditionally, it measures the properties of reflection or transmission of materials in the electromagnetic range, from UV to infrared (liquid or solids). The detected spectra show the absorption of the sample at a specific wavelength. For example, West *et al* [74] used a UV–Vis spectrometer during the development of the flashlamp-based photonic sintering of silver ink. To heat the ink with light, it is important that the ink layer has a thickness adapted to the wavelength of this light to allow a certain transparency on the whole thickness of the sample. Consequently, it is important to know the absorption of the ink at the specific wavelength of the light. The results obtained determine the acceptable thickness of the deposited silver ink beyond which the light will no longer penetrate and complete the sintering of the printed pattern. The UV–Vis–NIR spectra indicate the evaluation of the ink composition with the drying process [64, 75, 76].

In addition, during sintering/drying, the reflectivity of a silver thin film changes as the coalescence of the metal nanoparticles creates a surface reminiscent of a bulk metal [75, 77, 78]. Zenou *et al* [77] utilized a reflection probe coupled to a fibre spectrometer to monitor the spectral reflectivity as a potential non-contact technique. The obtained spectra coupled to an effective medium model can be used to calculate the resistivities of silver thin film. Therefore, the spectral reflectivity allows the monitoring of the evolution of the sintering process. Other groups have demonstrated the application of the reflectance spectra to convert them into colour coordinate values [78]. This is the principle of calorimetry, which is widely used in graphic printing applied to PE. Calorimetry has been used by the graphic printing industry to verify small changes in ink colour, as described in section 3 [13, 79]. The resulting reflectance values were fitted to a 3D colour space called CIELAB [46]. This approach quantifies any colour change, which is related to the strength values of the sintered ink sheet at different stages.

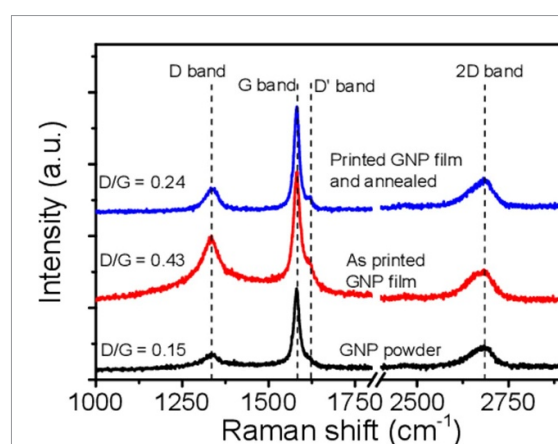


**Figure 13.** Raman spectra from the starting GNP powder, as-printed, and annealed ( $350\ ^\circ\text{C}$ ) GNP pattern. Reprinted with permission from [61]. Copyright 2019 American Chemical Society.

With UV–Vis–NIR spectroscopy being an efficient and well-developed technique, researchers have extended this range to infrared and far-infrared wavelengths. Fourier transform infrared spectroscopy (FTIR) is another very frequently used tool for the identification of functional groups incorporated in a newly formulated ink [76, 80]. The principle is the same as that of other spectroscopy techniques, which mainly measure the absorbance of a sample in the targeted wavelength range. This technique can be used for both solid and liquid materials.

Identification of the chemical composition of an ink is achieved by Raman spectroscopy, which provides the structural fingerprint of the vibrations of the triggered molecules [53, 61, 81, 82]. An example is shown in figure 13, where the intensity of the three main graphite bands (2D, G, D) varies in the graphene-nanoparticles powder (GNP) ink formulation. Figure 13 also illustrates the spectral evolution from GNP powder (black trace) to printed GNP films (red trace) and annealed film (blue trace) [61]. The structural change in the GNP planes is indicated by the change in the ratio of D and G bands (D/G). For example, the higher D/G value for the as-printed GNP film indicates an increase in GNP density during the formulation process. After annealing, the D/G

decreases, indicating a reduction in density of the graphene flakes and the removal of the polymer. Raman spectroscopy is essential for tracking chemical and structural changes during the ink formulation process [61].

All the techniques discussed above are optical light-based techniques. The surface properties can be obtained by the nanoindentation method, which is capable of defining the extent of solidification by probing the mechanical properties of thin films [56, 82, 84]. Typically, it measures the Young's modulus and the hardness. These parameters also allow the identification of an ink composition that has matching conditions with a substrate [82, 84].

#### 4.1.2. Current characterization technique for in-line printing

The in-line imaging ellipsometer has been actively used to measure the production thickness of printed electronic devices in the visible and ultraviolet spectral regions [31, 50, 85]. The principle underlying the technique is based on the evaluation of the polarization change of the light reflected by a printed layer [85]. Relative to the plane of incidence, the light can be decomposed into its orthogonal polarization components  $s$  and  $p$ . By normalizing the reflected  $s$  and  $p$  intensities ( $r_s$  and  $r_p$ ) with their incident values, the complex reflectance ratio can be calculated. Typically, the complex reflectance ratio  $\rho$  is expressed as [85]:

$$\rho = \frac{r_p}{r_s} = \tan \Psi e^{i\Delta}, \quad (5)$$

where  $\Psi$  and  $\Delta$  are ellipsometric parameters. The measured data are usually fitted to an appropriate physical model to provide the optical properties and thickness of the sample.

Ellipsometry is based on self-normalized measurements, meaning that it does not require a reference beam. It therefore provides fairly accurate and reproducible extracted values while being relatively insensitive to scattering and fluctuations. For in-line characterizations, Huemer *et al* [85] proposed to use a Single Crystal Photo-Elastic Modulator (SCPEM), which is a piezo-electric material. It modulates the polarization of the incident light by its stress-induced birefringence (photo-elastic effect). This technique illuminates the sample with four different polarizations, resulting in four recorded intensities. By applying appropriate fitting, the sample's thickness can be extracted.

To our knowledge, ellipsometry is the only in-line measurement used for characterizing PE production [50]. Indeed, this field of research is still in its infancy, and it is likely that other techniques will be added in the years to come.

#### 4.1.3. Post-printing characterization

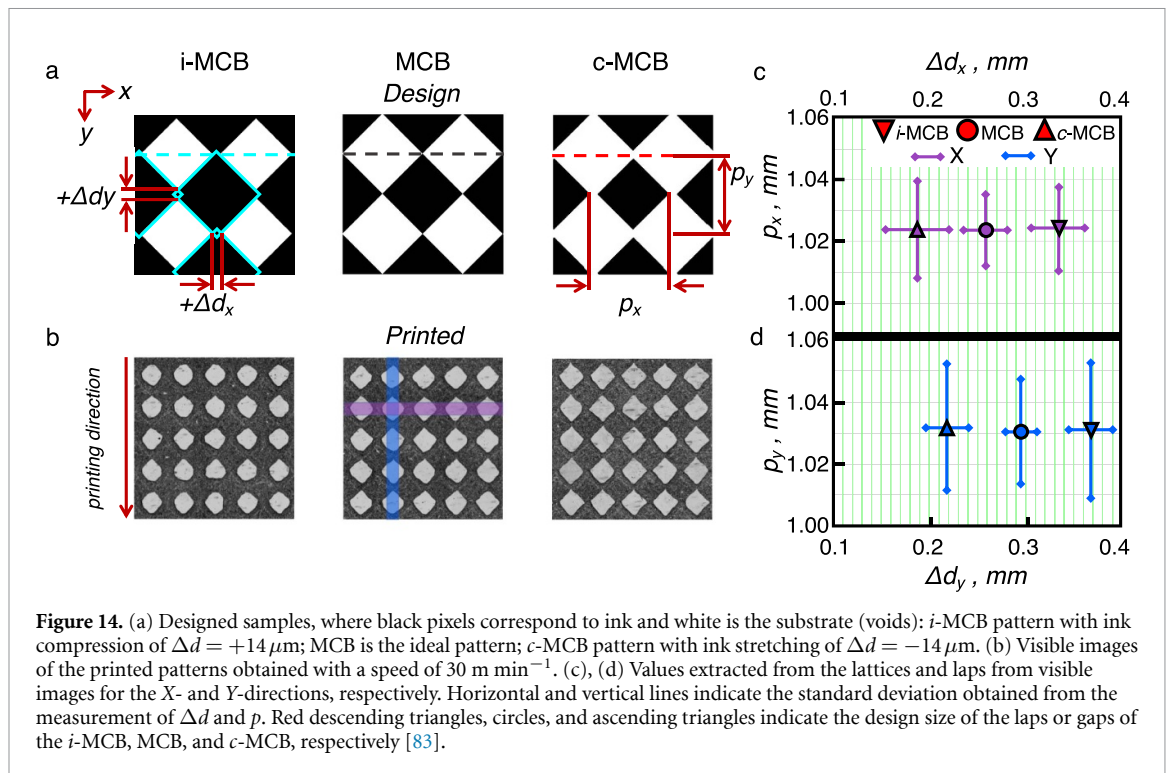
While the online methods are mainly dedicated to the characterization of the PE printing process, a

plethora of offline measurements are available to evaluate PE device functionality and print quality. Visual inspection is commonly used for PE quality control, and more specifically, with optical microscopy (OM), which is a widely used method for evaluating traces or printed devices. Standard compound OM is a common technique as it is relatively simple to capture a surface [23, 31, 32, 36, 40, 45, 82, 87–89], while confocal microscopy is used to provide three-dimensional (3D) information at the micrometer level [40, 59, 67, 82, 83, 87, 90].

Microscopic images are usually taken at each stage of production, from ink development [31, 32, 40, 87], substrate preparation [82], the deposition process [23, 59, 67, 83, 88, 89], to sintering/drying [32, 33, 36, 45]. This is particularly useful for characterizing the nature of crack formation [36] or for detecting different types of defects such as impacted droplet boundaries, the wetting phenomenon, irregularities, pinholes, etc [40, 90]. Often, computer-assisted image analysis is required, as small variations are not easily detected by the naked eye. For example, the work of Kim *et al* [67] introduced a printability and desired performance achievement factor between the target pattern and the printed pattern. It calculates the number of overlapping pixels between the drawn pattern and the printed pattern. The number obtained refers to the presence of defects due to the variation induced in the printing process.

Similarly, Zhuldybina *et al* [83] studied the printed metal checkerboard (MCB) pattern to extract lattice parameters using OM images with image post-processing, as shown in figure 14. The designed and printed images are shown in figures 14(a) and (b), respectively. The visible observation between the MCB and  $c$ -MCB structures shows almost no difference. However, counting the number of black or white pixels to extract the lattice ( $p_x$ ,  $p_y$ ) and gap ( $\Delta d_x$ ,  $\Delta d_y$ ) sizes for the X- and Y- directions shows the difference in the printed structures. As shown in figure 14(b), the rectangular areas shaded in purple and blue identify the extraction areas for tracking connection sizes in the X- and Y- directions, respectively. The results obtained are summarized in the figures 14(c) and (d), which shows that the gap sizes and lattice parameters differ in the two directions of each structure, as well as between them. The main disadvantages of these imaging techniques are that they require access to the near field of the sample to be imaged (i.e. they need to be very close to the sample) and that information extraction is time consuming.

AFM is also an image-based technique providing a nanometer-scale resolution. However, it can only measure areas with side lengths in the order of a hundred microns and heights in the micron range [91, 92]. Another way to study roughness, film thickness and surface morphology over a larger area ( $\sim$ few  $\text{cm}^2$ ) is through the use of profilometers. Profilometry can be done either using a physical contact



or using light. The contact method or stylus profilometry (SP) works mechanically, similarly to AFM, and is a destructive QC method [37, 40, 60, 66]. Indeed, the interaction force between the probe/tip of SP and the sample surface is strong enough to create potential cracks in soft (poorly sintered) samples. This can lead to a misinterpretation of the measurements. On the other hand, optical profilometry (OP) is a non-contact technique for precise measurements of a surface profile [88, 91, 92]. There are different variations and principles of microscopy applied to OP, such as interferometry, scattering, and confocal laser scanning microscopy [91, 92]. SP and OP measure an area of a few cm in a short time frame. SP is mostly used for thickness measurements, while OP can also be applied for surface roughness characterization [33, 37, 40, 44, 60, 66, 89, 92, 93].

As mentioned earlier, the conductivity of printed inks must be as high as possible to allow for the conduction of electrical current with the least amount of loss. Typically, to extract this parameter, another means must be used to evaluate the resistivity, or sheet resistance. To date, the multimeter and/or four-point probe (4PP) are widely used for these measurements in the PE industry [33, 37, 59, 60, 66, 82]. A typical example of these devices is shown in figures 15(a) and (b).

Figures 15(c) and (d) depict the schematic configuration for the resistance measurements for the multimeter and 4PP method, respectively. The multimeter, which is easy to manipulate, uses only two probe contact resistance measurements. However, the resistance of the multimeter wire causes a considerable error of up to 20% [86]. 4PP is broadly used in

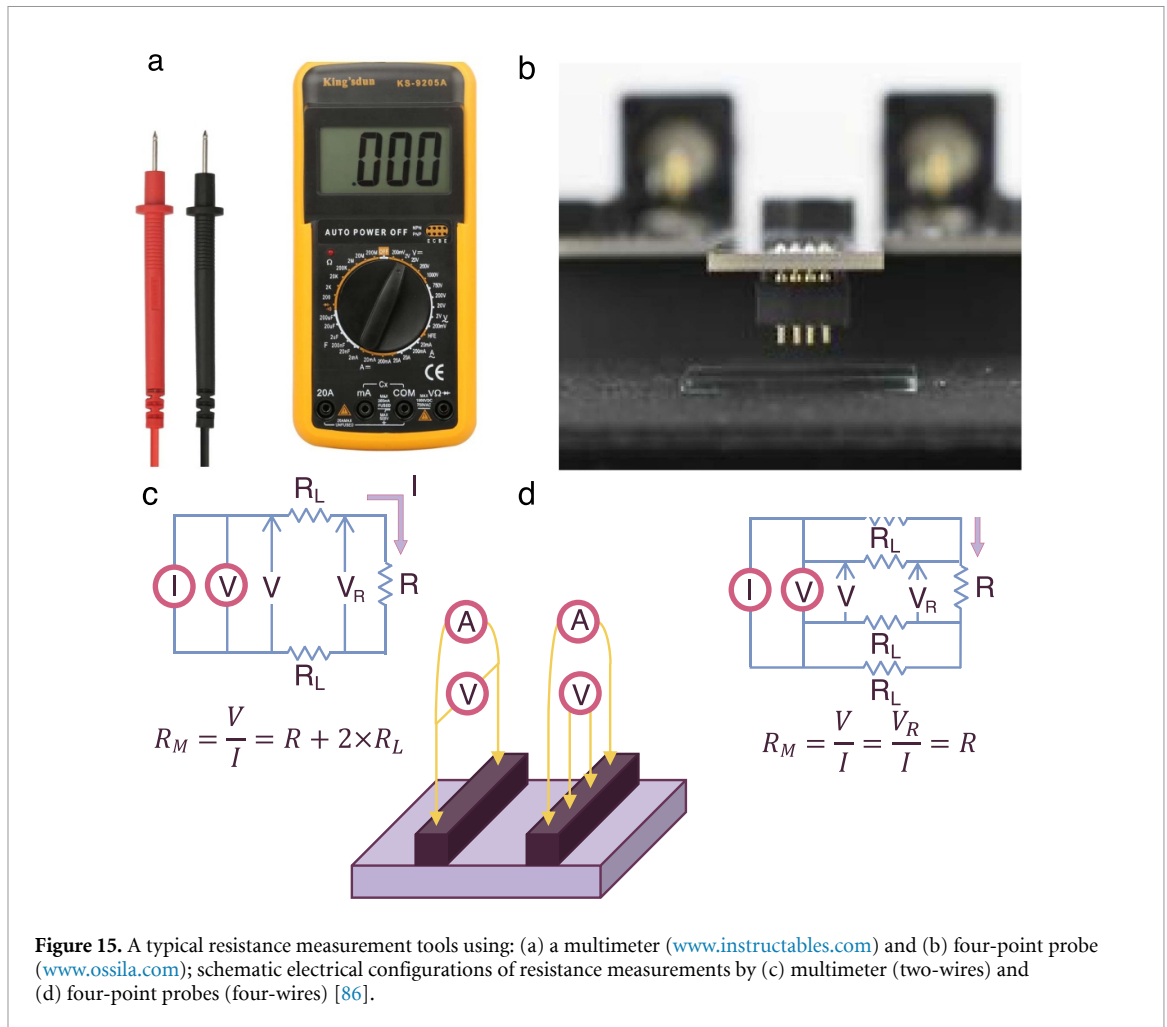
the lab environment, and consists of four equidistant contacts in a line, where the outer contacts are connected to a current source and the inner contacts are used to measure the induced voltage [86]. In fact, the 4PP provides a more accurate resistance value due to the presence of both sets of leads testing and sensing at the same time. A geometric correction factor is usually required to convert the voltage/current ratio measured by the 4PP into sheet resistance. This correction factor accounts for the sample size, shape, and probe spacing [66, 94].

## 4.2. Emerging techniques

This section combines the latest non-contact techniques for PE production QC. This review shows a trend toward an in-line analysis process. Therefore, we have not categorized these methods by separate print process control stages, but simply by method. Although some of these methods are very old, their association with PE characterization is quite recent.

### 4.2.1. X-ray techniques

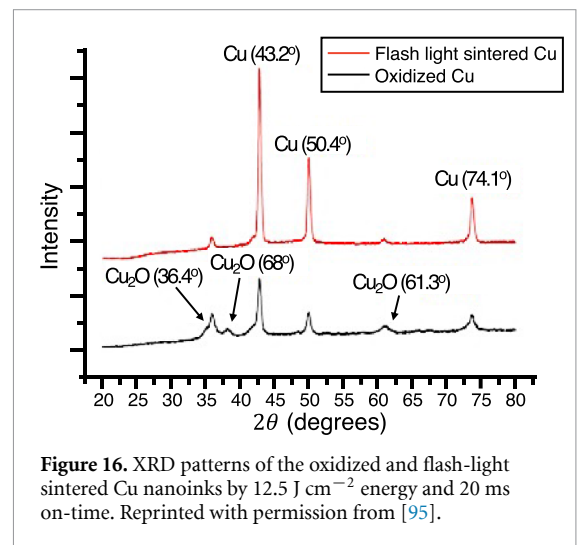
The use of electromagnetic waves to carry out the metrology of a sample has the clear advantage of being non-contact, and therefore, well adapted to an eventual in-line characterization. On the high frequency side of the electromagnetic spectrum, x-ray diffraction (XRD) is a well-known non-destructive method for monitoring the structural and compositional properties of printed layers [36, 41, 45, 53, 95, 97]. A standard database for x-ray diffraction patterns enables a quick identification of atoms combining structures with preferred crystal orientations (texture) and other structural



parameters, such as average grain size, strain, and crystal defects [98].

As shown in figure 16, XRD can be applied to study the sintering mechanism by comparing the diffractogram before and after sintering [36, 41, 45, 53, 55, 95, 97]. Since the presence of metal oxide is decreasing within applied sintering, the peaks corresponding to metal oxides (black curve in figure 16) eventually decrease their intensity drastically or fully disappear [95].

Dam *et al* [99] implemented a small angle x-ray scattering (SAXS) to analyze the crystallinity of a P3HT:PCBM (semiconductor material) bottom cell during coating of the different layers of the stack. Figure 17 sketches the experimental system, where a small R2R coating machine was placed into SAXS system with a total size of  $\sim 6$  m to obtain an incidence angle of  $0.35^\circ$ . R2R was operating at the speed of  $0.5 \text{ m min}^{-1}$ . Ptychographic data (i.e. images obtained by processing many coherent interference patterns) of each layer were extracted *in situ* during coating conducted at a controlled distance from the x-ray probe point, allowing measurements at a position with a constant wet layer thickness. By combining phase projections from different angles, the 3D distribution of x-ray refractive indices was obtained. As



is shown at the bottom of figure 17, the different scattering signals indicate the crystalline structures of each layer. This approach has been widely applied to study the interaction of the overcoating of several functional layers in organic tandem solar cells, and ptychography data has provided insight into a complete 12-layer solar cell stack [26, 52, 99, 100].

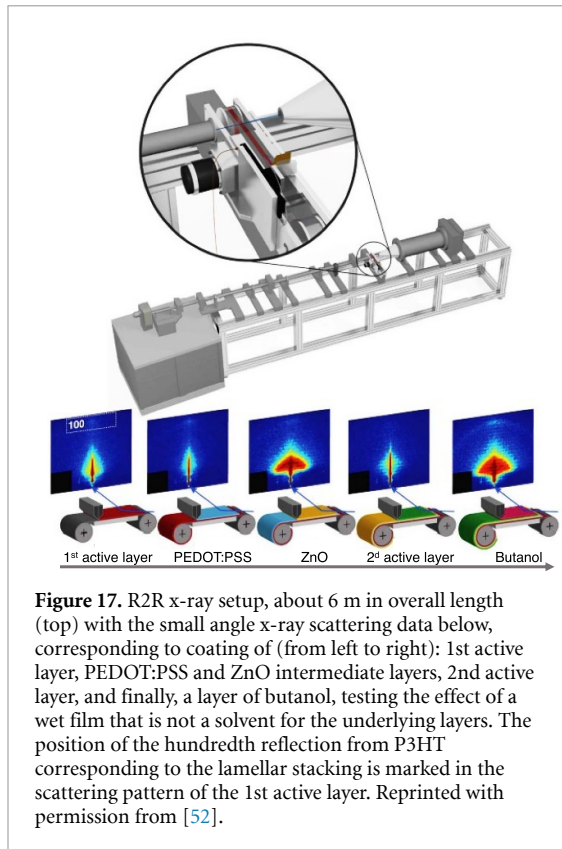


**Figure 17.** R2R x-ray setup, about 6 m in overall length (top) with the small angle x-ray scattering data below, corresponding to coating of (from left to right): 1st active layer, PEDOT:PSS and ZnO intermediate layers, 2nd active layer, and finally, a layer of butanol, testing the effect of a wet film that is not a solvent for the underlying layers. The position of the hundredth reflection from P3HT corresponding to the lamellar stacking is marked in the scattering pattern of the 1st active layer. Reprinted with permission from [52].

Rossander *et al* [101] also used this approach for controlling the different stages of sintering.

#### 4.2.2. All-optical difference engine (AODE)

X-ray is not the only part of the electromagnetic spectrum that is used for quality control of PE. The most accessible spectral range used is certainly the visible range, from 400 nm to 800 nm, simply because images can be detected using highly available optical systems with standard cameras.

For example, an all-optical difference engine (AODE) sensor is used for in-line defect detection by counting the number of pixels [96]. As shown in figure 18, a sample is illuminated with a continuous wave laser located in the visible range. After passing through the AODE, the light is detected with a complementary metal oxide semiconductor (CMOS) image camera, which receives the optical difference image. AODE combines two lenses ( $L_1$  and  $L_2$ ) with a focal length of 75 mm (in a 4f imaging configuration), and with an amplitude grating in between them. This system works based on a coherent optical subtraction using 1D-spatial filtering between neighbouring objects at a defined distance  $2d$  as depicted in figures 18(a)–(d).

Figure 19(a) shows an image of a printed reference and defective pads after applying a subtraction. Figures 19(b) and (c) are the results captured by AODE for a condition without defect. Figures 19(d) and (e) are the saturated images of defective and reference pads, which are used to identify

the threshold limits: defect and defect-not-detect, respectively. To eliminate the use of a bulky image post-processing and to simplify the overall system, a photodiode can be used instead of a camera. In this case, a saturation threshold can be applied, and only the saturated pixels will be recorded, which indicates the presence of a defect.

#### 4.2.3. LED-based optical inspection

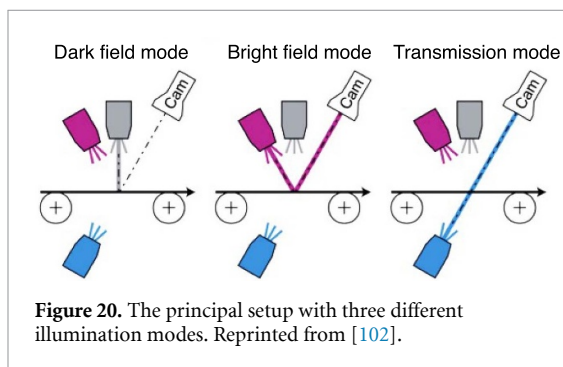
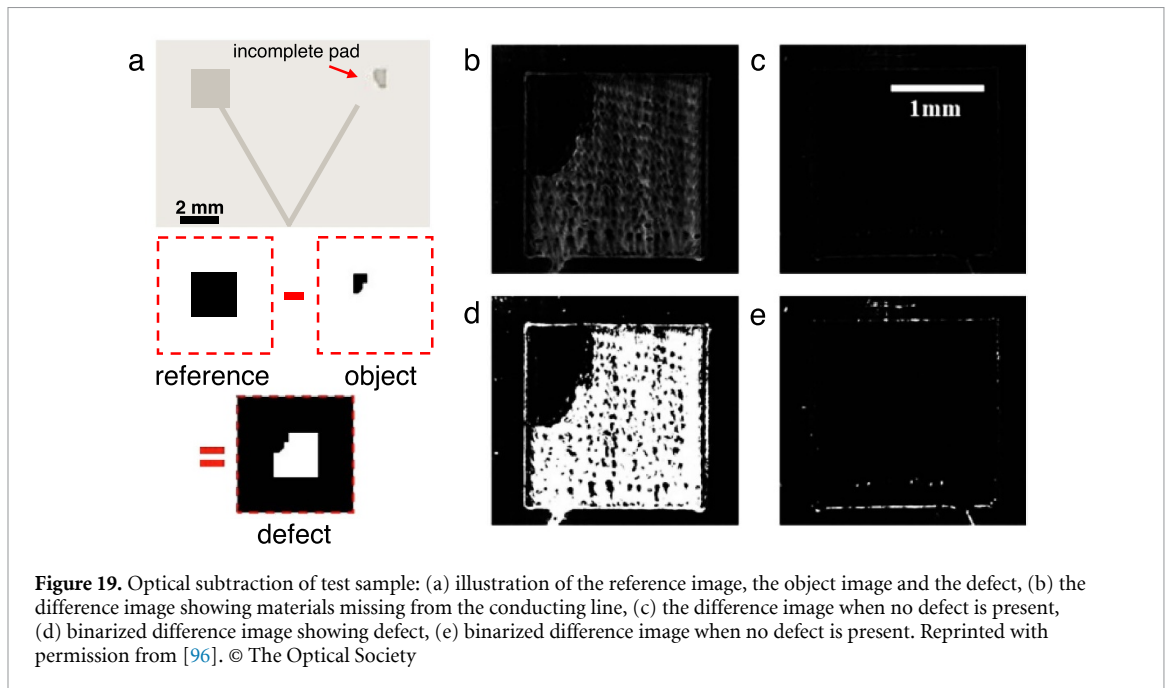
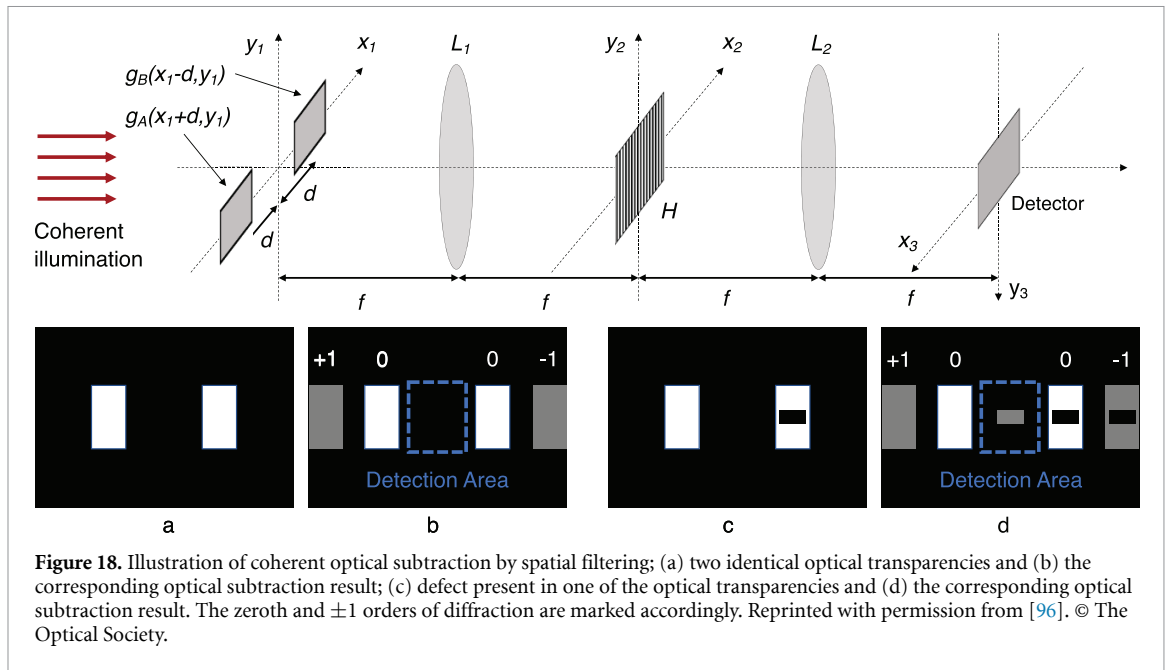
To ensure the quality of printed single layer or multilayer devices, an analysis of potential defects is essential. Espinosa *et al* [102] employed an optical inspection system (SolarInspect RtR, Dr Schenk GmbH, Germany), consisting of LED-based light sources (white, red, blue) with two 8192 pixel line-scan cameras. This system allows simultaneous observation in transmission mode, dark field and bright field using different light sources. For the production of multilayer devices, each layer may have different transmission or reflection properties. A particular light source was applied, depending on the type of surface, e.g. transparent or opaque, thin or thick.

Figure 20 shows the in-line inspection system of different solar cell layers based on three different illumination modes. The bright-field (red LED) and transmission modes (blue LED) are well suited for the thin and semi-transparent films, while the dark mode (white LED) is used for the thick and rough surfaces. The camera output is overviewed in figure 21 at a production speed of  $20 \text{ m min}^{-1}$ . For example, PEDOT:PSS electrodes have been screen-printed, hence, it is a thin and semi-transparent layer.

Typical defects for screen-printing such as pinholes are clearly visible in transmission mode (last column of figure 21) as white dots, while in the bright field (third column of figure 21), pinholes create optical bangs around them. The inspection of a stacked layer of PEDOT:PSS with ZnO and an active layer with the bright field mode of different thickness also create the optical fringes. This helps to identify short circuits in the final product. The dark field mode (second column in figure 21) was used for the final printed layers, which have a thick and rough surface. It shows the quality of the edges, pinholes, and interconnections between layers. The combination of all modes allows the inspection of all fabricated layers and the detection of potential defects to ensure high device functionality.

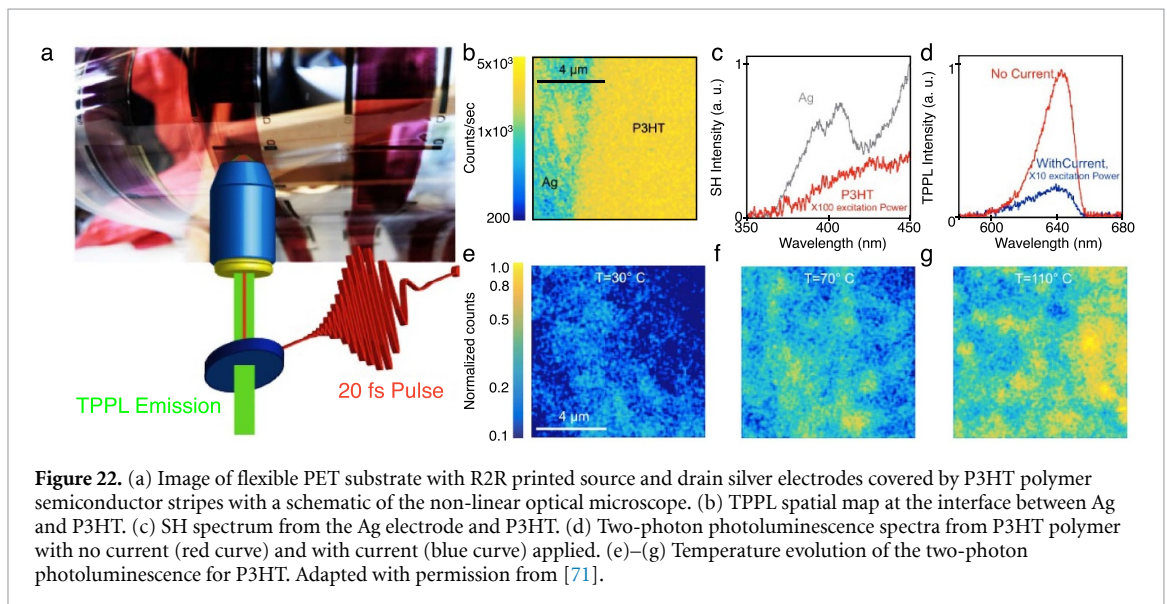
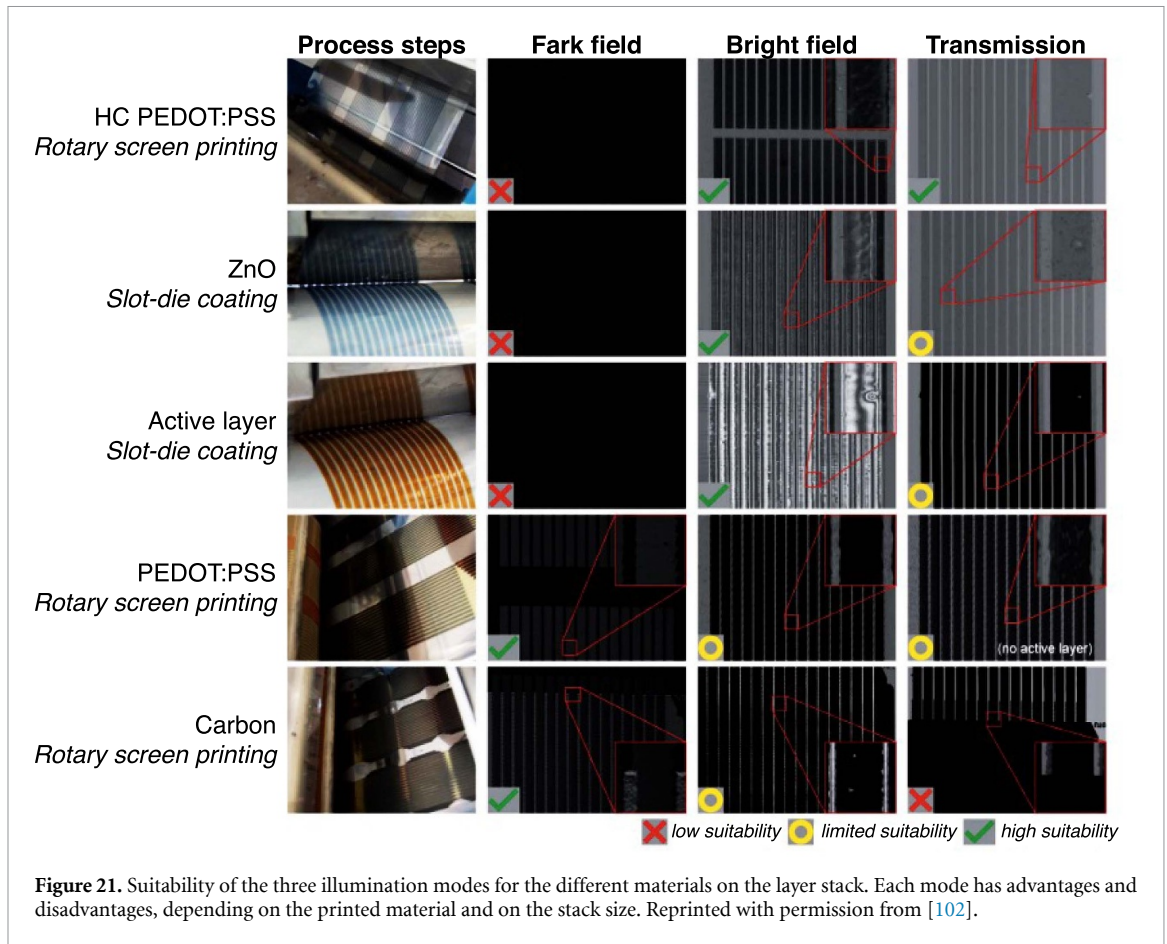
#### 4.2.4. Non-linear optical microscope

Pasteoreli *et al* [71] characterized a roll of polymeric semiconductor material deposited on a flexible substrate by nonlinear microscopy, as shown in figure 22(a). An ultrashort (20 fs) pulsed laser probe in the near infrared ( $\sim 800 \text{ nm}$ ) stimulates two-photon absorption in a semiconductor layer, resulting in induced two-photon photoluminescence (TPPL) and a second harmonic (SH) response, which are recorded with a photodetector [71]. 2D



images are mapped by a photodetector as the sample is scanned. The different types of nonlinear responses allow to discriminate between conductive

(Ag) and semiconductive (P3HT) materials, as shown in figure 22(b). The 2D image was acquired by continuously exciting the sample with ultrashort pulses and detecting the nonlinear intensity; in this context, a low intensity on the left side is attributed to Ag electrodes, and on the right side, the high intensity is related to P3HT. The spectral information of SH is shown in figure 22(c), where Ag shows a strong peak at 400 nm, which corresponds to the wavelength of the SH from an 800 nm laser beam, while P3HT has a very weak signal. The double peak in the spectrum for Ag is explained by a non-perfectly compressed pulse. Figure 22(d) shows the TPPL spectra of the P3HT with and without current applied between the source and drain. The intensity difference is a factor of 4 between zero and the applied current (ten



times higher power). Furthermore, this method was applied to measure the effect of temperature on the P3HT TPPL intensity for 30 °C, 70 °C, and 110 °C, as shown in figures 22(e)–(g). From these figures, it is clear that the TPPL signal increases with temperature indicating the change in the molecular packing and, hence, in charge carrier density. The relationship between the molecular packing and carrier density of the active material with the TPPL signal

intensity indicates the ability of nonlinear microscopy to extract fundamental physical parameters of PE devices.

#### 4.2.5. Eddy current testing

Non-destructive testing (NDT) using capacitive and eddy current sensors is broadly used for defect detection in semi-finished products, e.g. wires, bar, and tubes in the production line [93, 103, 104].

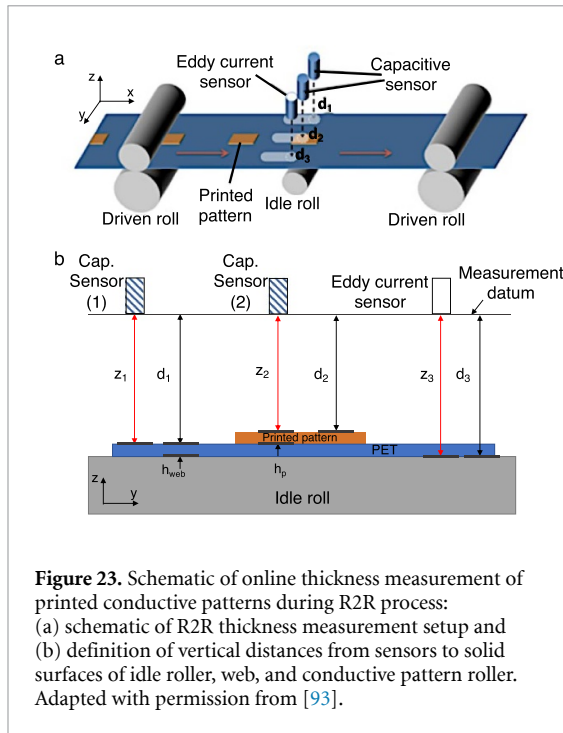


**Figure 23.** Schematic of online thickness measurement of printed conductive patterns during R2R process: (a) schematic of R2R thickness measurement setup and (b) definition of vertical distances from sensors to solid surfaces of idle roller, web, and conductive pattern roller. Adapted with permission from [93].

Seong *et al* [93] used a combination of two sensors for in-line and non-contact thickness measurements of conductive ink adaptable to an industrial printing process such as R2R. Figure 23(a) shows that the design module is placed on top of the printing web, while an idle roller is placed underneath to minimize the fluctuation of the printing web. The design module, which contains two capacitive sensors and an eddy current sensor, allows *in-situ* thickness measurements. To obtain accurate thickness measurement results, both types of sensors are used simultaneously. Capacitive sensors measure only the surface, without penetrating the material. As shown in figure 23(b), sensors 1 and 2 measure the distance to the substrate ( $d_1$ ) and to the printed layer ( $d_2$ ), respectively. By looking at the difference between the two, the thickness can be determined. However, capacitive sensors are very sensitive to changes in the dielectric constant, which can occur due to dust, air quality, etc. It is therefore necessary to perform an additional measurement using an eddy current sensor, shown as sensor 3 in figure 23. It uses the magnetic field for detection, which is not affected by non-conductive contaminants. In addition, it eliminates any fluctuation in measurements with capacitive sensors. The eddy current sensor measures the distance ( $d_3$ ) between the sensor and the idle roller. Combining the data from the three sensors, the following thickness results are obtained:

$$h_p = D_{1a} - D_{2a},$$

$$\text{where } D_{1a,2a} = \frac{1}{N} \sum d_{1i,2i} + \frac{1}{N} \sum d_3 - d_{3i}, \quad (6)$$

where the subscript  $i$  means the the  $i$ th data point of the sensor output and  $N$  is the number of data points.

This measurement results in a 20% runout error at the print speed of  $3 \text{ m min}^{-1}$  (e.g. a trace width of about  $5 \mu\text{m}$  with an accuracy of  $1 \mu\text{m}$ ).

Lewis *et al* [104] used the eddy current approach for conductivity measurements. Figure 24(a) sketches the experimental setup used to measure the conductivity. A typical sensor and the printed traces are shown in figures 24(b) and (c), respectively. An alternating current flows through the sensor coil, creating an alternating magnetic field around it. When this magnetic field interacts with a conductive target, it induces an eddy current, which produces its own magnetic field. This generated magnetic field is opposite to the initial one, which lowers the net magnetic flux at any depth. As a result, the eddy current concentrates at the surface, closer to the coil, and the current density decreases exponentially with depth. This depth at which the eddy current density decreases as  $1/e$  is referred to as the standard depth of penetration ( $\delta$ ) and can be given as follows:

$$\delta \approx \frac{1}{\sqrt{\pi f \mu_0 \mu_r \sigma}}, \quad (7)$$

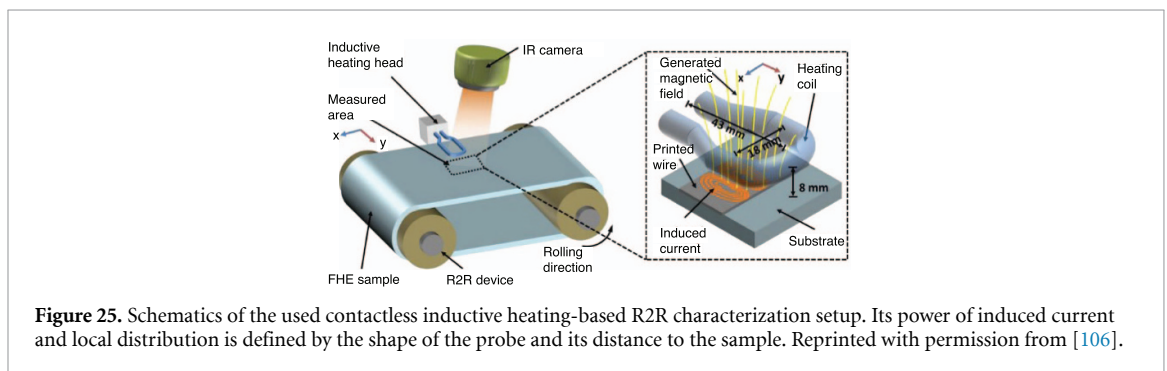
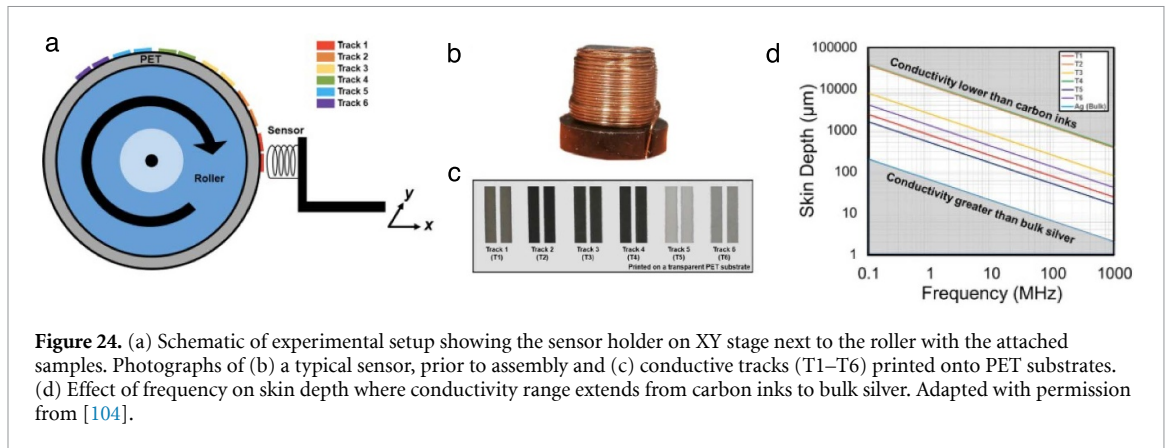
where  $\mu_0$  and  $\mu_r$  denote the vacuum and relative magnetic permeability,  $f$  is the frequency of the sensor, and  $\sigma$  is the electrical conductivity of a tested sample.

Equation (7) highlights the importance of choosing the proper sensor frequency to increase the penetration depth, and hence, to reduce the effect of thickness when measuring electrical conductivity. As shown in figure 24(d), a higher frequency results in a lower penetration depth into a conductive surface and vice versa. To identify the most appropriate coil to operate in a PE production environment, the experiment was carried out with coils having different resonance frequencies. It was determined that the coil with a diameter of 7 mm operating at 5.5 MHz has resistivity measurements in the range of interest for PE ( $10^{-6}$  to  $6.3 \times 10^{-4} \Omega\text{m}$ ). Even with an operational speed of up to  $80 \text{ m min}^{-1}$ , the eddy current approach was able to detect resistivities of  $0.1 \Omega\text{sq}^{-1}$  to  $1.6 \Omega\text{sq}^{-1}$ .

#### 4.2.6. Thermography

In the synchronized thermography (ST) technique, samples are heated with direct current (DC) and synchronized with infrared (IR) imaging to produce thermograms [72, 105]. The generated images illustrate the nonuniformities of conductive thin films, particularly nonuniformities in electrical conductivity, that will influence the current density, thus modulating the temperature distribution as a function of conductivity uniformity.

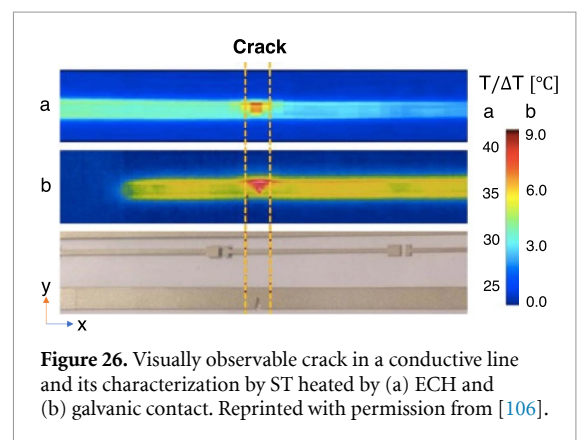
In order to apply ST to online measurements of flexible hybrid electronics (FHE), Remes *et al* [106, 107] proposed to use induction heating based on the eddy current method (ECH), as shown in figure 25. Eddy currents inside the test specimen



are generated by placing the oscillating magnetic field near the specimen. This oscillating magnetic field is produced by exciting the conducting wire (coil) with an alternating current. The induced current is used for the electrical heating of ST, and is recorded with an IR camera. This approach requires simple data processing to analyze the obtained thermograms.

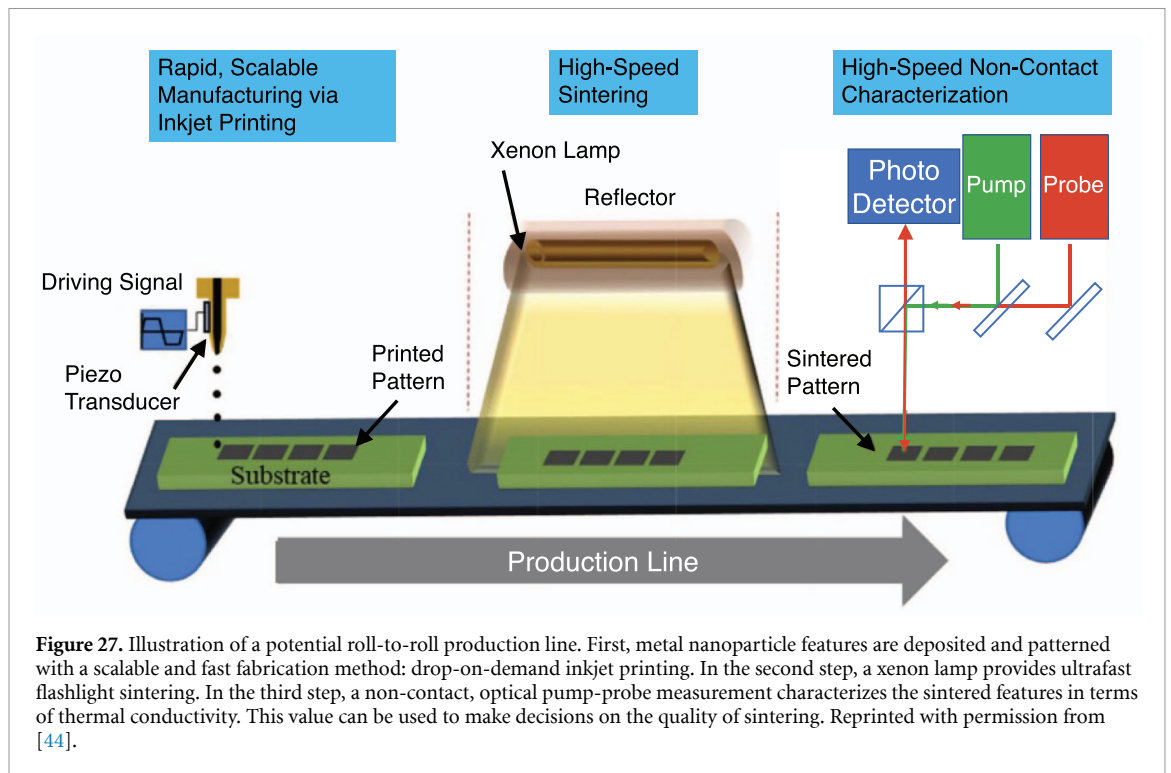
As mentioned above, the temperature gradient is a clear indication of the irregularity of conductive films due to thickness variations or defects [106, 107]. Figure 26 shows typical thermograms obtained by (a) ECH and (b) by galvanic contact. Regardless of the heating method, the defect induces a temperature rise since it leads to a reduction of the cross-sectional area, and thus an increase of the current density on the remaining part. The absolute temperature rise is limited by the type of heating. The ECH-based non-contact ST measurements were performed at a printing speed of  $2 \text{ m min}^{-1}$ .

Frequency-domain thermoreflectance (FDTR) is based on measuring the thermal conductivity of conductive layers, which are heated with infrared radiation [44]. Figure 27 illustrates a possible application of FDTR-assisted R2R production. A frequency-modulated pump laser creates a heat flux at the sample surface due to the absorption of pump light by the sample. The periodic heat flux causes temperature oscillations. A probe laser that is not modulated



measures the reflectivity of the sample as a function of temperature. A lock-in amplifier is locked to the frequency of the pump laser. Thus, the thermal phase of the pump laser is recorded. The phase information is then fitted to a thermal model to extract the thermal properties of the samples related to their conductivity [44].

**4.2.7. Terahertz time-domain spectroscopy (THz-TDS)**  
Over the past 30 years, the development of terahertz (THz) technology has opened up many opportunities for quality control in industry for on-line and non-destructive testing (NDT) [108–110]. THz radiation corresponds to the 0.1–10 THz frequency range, which in turn correspond to a 0.03–3 mm



wavelength range and a photon energy of 1–10 meV. THz radiation is transparent for many types of optically opaque non-conducting or organic materials, making THz spectroscopy a versatile tool for studying material properties thanks to its non-contact, non-destructive, high-resolution, and non-invasive capabilities [111–113]. Unlike x-rays, THz detection allows non-ionizing detection due to its low photon energy.

To control the quality of conductive PE layers, Zhuldybina *et al* [83, 114] introduced a simple strategy using a THz resonant structure as a quality control bar (QCB) for printing and characterized it by THz time-domain spectroscopy (THz-TDS). The main part of the THz-TDS system is a femtosecond (fs) laser, which, through an emitter, transforms the fs pulse into a picosecond THz pulse [115]. The authors used photoconductive antennas (PCAs) for THz beam emission and detection. That strategy allows the non-destructive testing of the condition of a PE production line in the same way as with traditional graphic printing, as described section 3 [47], but with the added possibility of obtaining the functionality of the ink. To ensure the interaction of the THz beam with the conductive ink, QCBs are fabricated as THz metasurfaces (MSs). These MSs exhibit a strong resonant response in the THz frequency range, with geometries allowing transmission or reflection measurements. The resonance is proportional to the variation of the MS unit cell, its mesh, and other geometric parameters or material properties [116].

Existing printing techniques allow MSs to be printed with spatial resolution in the range of 10–100  $\mu\text{m}$  (see table 1). A key point of this strategy is the small printing area (e.g. 1  $\text{cm}^2$ ) required to recover the properties of the ink and printing parameters during the production of PE devices. This method requires recording the transmission signal from a sample (QCB) and a reference (substrate or air).

As shown in figures 28(a) and (b), the normalized transmission of two types of MSs is presented. Figure 28(a) shows the variation of transmission as a function of conductivity and figure 28(b) shows the variation of transmission as a function of the size of the neighbouring diamond connections resulting from the spread or shrinkage of the printed patterns relative to a designed pattern. Both spectra highlight that these changes in ink quality can be identified from the maximum or minimum transmission at the resonant frequency of the designed MS. Figures 28(c) and (d) show the agreement of the THz results with conventional techniques and the inset in figure 28(c) shows the fit with the simulation results, which highlight the extremely high sensitivity of the THz-TDS measurements for the typical conductivity range of PE. More remarkably, THz-TDS measurements can track variations in conductivity, geometric accuracy of the print, and the amount of ink deposited from the printer, with a level of accuracy similar to, or even better than, that of conventional techniques.

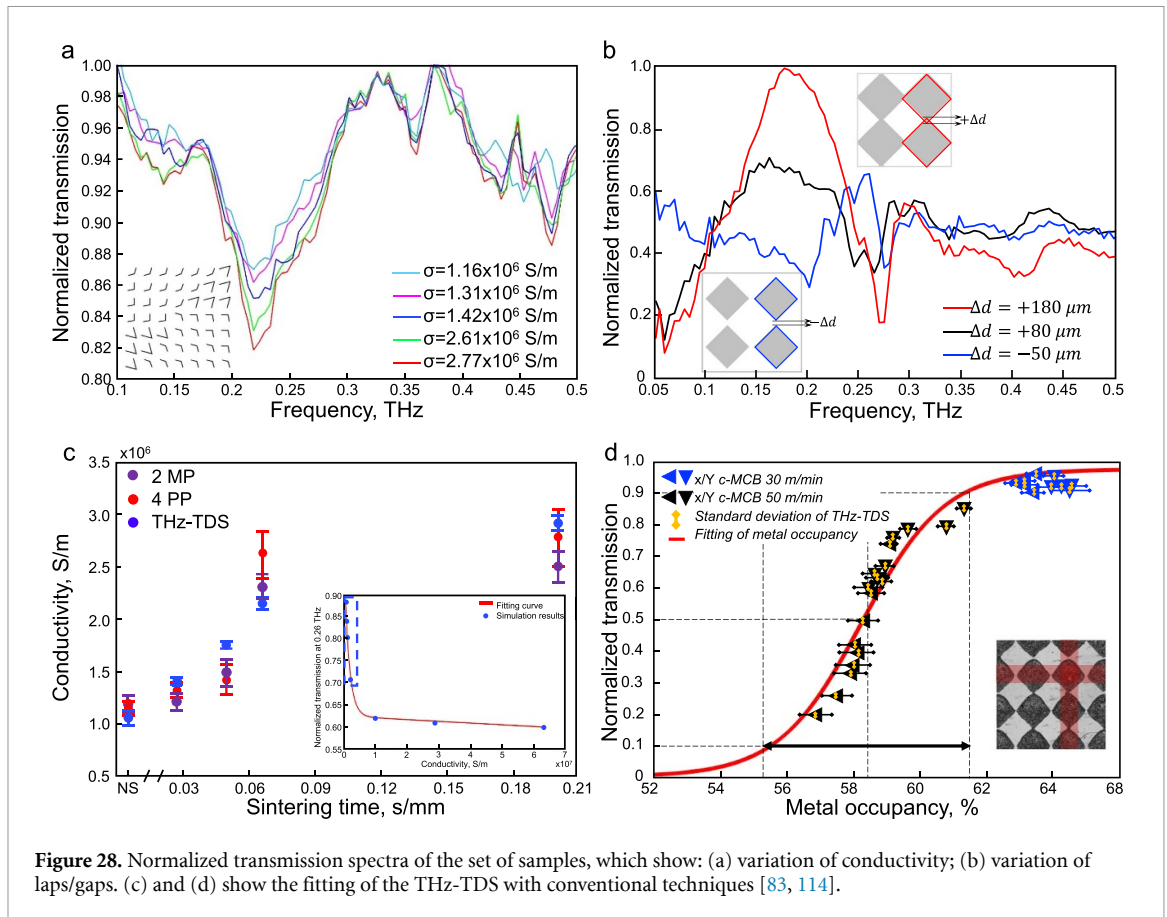


**Figure 28.** Normalized transmission spectra of the set of samples, which show: (a) variation of conductivity; (b) variation of laps/gaps. (c) and (d) show the fitting of the THz-TDS with conventional techniques [83, 114].

#### 4.2.8. Terahertz imaging

Zhang *et al* [117] inspected the surface uniformity of printed inks using THz imaging and the system resolution. Figures 29(a) and (b) show the photo and a sketch of the experimental setup, respectively. The 100 GHz source is an IMPact ionization Avalanche Transit-Time (IMPATT) diode, and the detector is a GaAs HEMT (high electron mobility transistor)-based line scanning array from Terasense Ltd. A tested sample was placed on the side of a 1D slider, where the line scanner array is located orthogonally just beneath the slider (less than 1 mm) to produce a 2D near-field imaging. The slider speed in this work was set at  $0.6 \text{ m min}^{-1}$ . The inset of figures 29(c)–(e) show photos of tested samples: silver ink printed on Teslin paper; silver ink printed on Teslin paper compressed by a mini roller mill to create the uniform printed area; an interdigital electrode printed with a silver ink on a PET substrate. The images of the amplitudes obtained at 100 GHz and transmitted through these samples are shown in figure 29(c)–(e), these have been normalized with the reference image at 100 GHz, i.e. without

any samples. The observation of printed ink on the paper shows that the lamination treatment significantly blocks the THz signal (see figure 29(d)). The results in figure 29(e) indicate some blue (blocked for THz waves) and red (transparent for THz waves) areas, which correspond to silver electrodes and PET, respectively. Even with a 3 mm spatial resolution of the detector, it was possible to identify conductive and non-conductive areas. This approach introduces the possibility of simultaneously obtaining dielectric and spatial information on samples [117, 118].

Finally, it should be mentioned that two-dimensional THz imaging capable of operating in real time generally requires more complex instruments than does a standard THz-TDS spectroscopy system. Even more complex instruments [119, 120] have been used to measure near-field PE devices [121], revealing defects with the micron-level spatial resolution. However, the near-field THz imaging method is not easily applicable for online QC of PE since the sensor must be in contact with a sample.

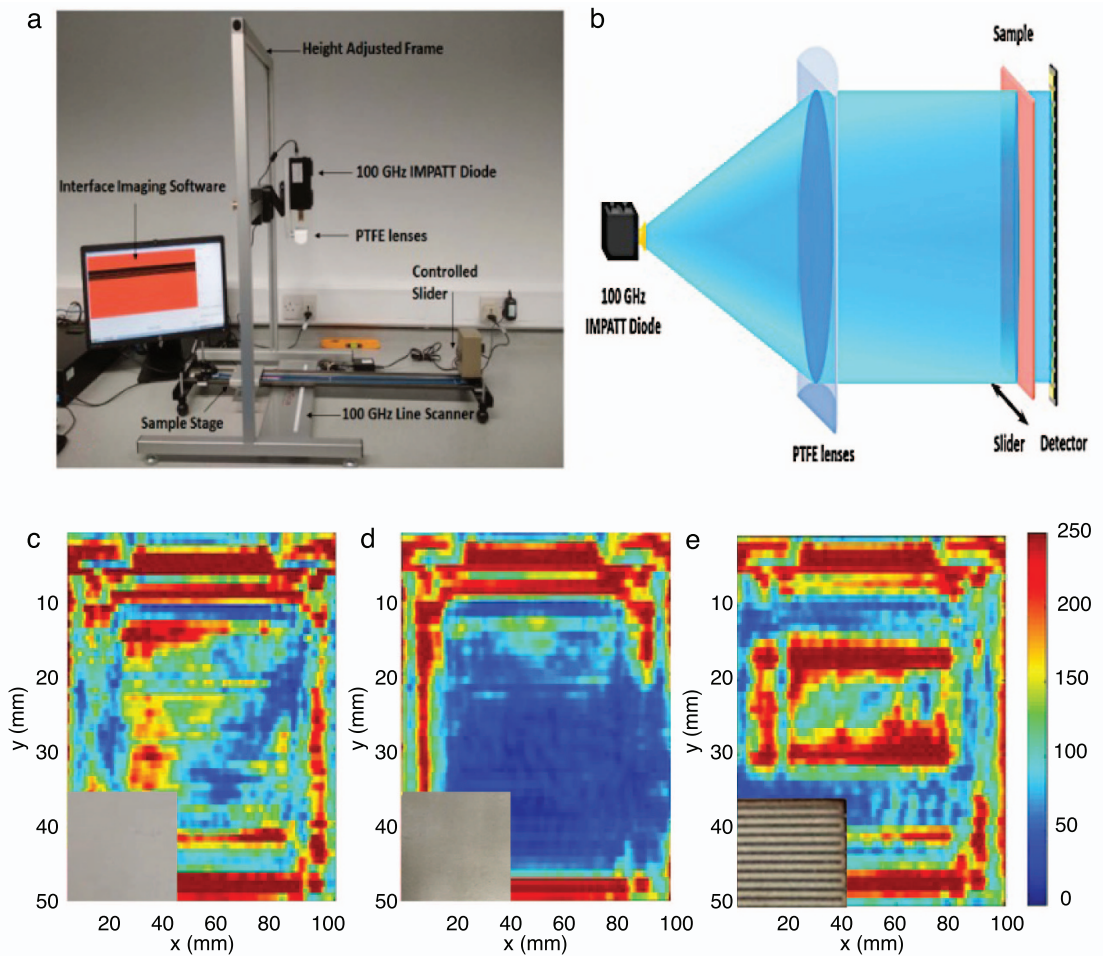


**Figure 29.** (a) Photograph and (b) schematic plot of the 100 GHz line scanning imager. (c)–(e) are images of transmitted amplitude information acquired from the mm-wave line scanner imager at 100 GHz for (c) printed silver ink on a Tesla paper substrate without rolling compression treatment after printing; (d) printed silver ink on Tesla paper substrate with rolling compression treatment after printing; (e) printed silver interdigital electrode ink on a thin polyethylene film substrate. The hot red colour indicates higher amplitude mm-wave signals transmitted through the samples and the dark blue denotes lower amplitude signals transmitted through the samples. Adapted with permission from [117].

## 5. Concluding remarks

The production of PE devices is rapidly evolving to encompass high-speed printing methods. However, the methodologies required to manufacture at high speed while keeping quality at a high level lag behind the immediate need. Despite the growing availability of characterization methods, the transition from the world of small-scale R&D to industrial mass production remains a hurdle to overcome. The most significant challenge at this time is the implementation of an active and real-time feedback directly into the process, which would be an extremely important advance at the industrial level. The present review has discussed some of the emerging techniques for non-destructive, in-line inspection of the printing process that may one day be implemented on a mass production line. A summary of the most important features of these methods is presented in table 3.

The identified emerging techniques can be divided into two categories: image analysis and signal

analysis, as shown in table 3. Image-based methods detect defects or extract conductivity from surface information, whereas signal detection systems measure calibrated values during production, which are then linked to actual physical information such as conductivity or geometry. All of the emerging techniques could potentially be incorporated into a closed-loop operation at different stages of print production. However, there is no technique which can control the final device performance. Similarly to the graphic printing industry, where high quality image inspection is necessary at the end of production, the PE industry will need to develop or implement a technique which can test the final device functionality.

It is interesting to note in this table that two methods could naturally be combined to provide a comprehensive characterization of a visual presence of defects and the PE production process: the **AODE** and **THz-TDS** quality control methods, respectively. An in-line inspection system based on pass or fail decision making could thus be possible. The natural

**Table 3.** Comparison of reported emerging techniques: AODE—all-optical difference engine sensor; LED—light-emitting diodes-based optical inspection; Non-linear OM—non-linear optical microscope; THz imaging—terahertz imaging; ECT—Eddy current testing; ST—synchronized thermography; THz-TDS—Terahertz time-domain spectroscopy; SAXS—small angle x-ray scattering.

Characteristics	Image analysis				Signal analysis			
	AODE [96]	LED [102]	Non-linear OM [71]	THz imaging [117]	ECT [93, 104]	ST [106, 107]	THz-TDS [83, 114]	SAXS [99]
Thickness sensitivity, $\mu\text{m}$	N/A	N/A	N/A	N/A	0.975	N/A	<1	N/A
Lateral resolution, $\mu\text{m}$	$\sim 10^{0*}$	10	0.4	3000	N/A	$10^3$	30	N/A
Geometrical parameters	N/A	N/A	N/A	✓	N/A	N/A	✓	N/A
Conductivity measurements	N/A	N/A	indirect	indirect	indirect	indirect	indirect	indirect
Defect detection	✓	✓	N/A	✓	N/A	N/A	N/A	N/A
Functional speed, $\text{m min}^{-1}$	$\sim 10^{1*}$	2	$\sim 10^{1*}$	N/A	80	2	$\sim 10^{1*}$	0.5
Pass/reject quality control	✓	✓	✓	N/A	✓	✓	✓	✓
Control of the process	✓	✓	✓	N/A	✓	✓	✓	✓
Device performance	N/A	N/A	N/A	N/A	N/A	N/A	N/A	N/A

\* Corresponds to expected (non-tested) approximate values

extension of this capability is the implementation of artificial intelligence (AI) assistance, in particular, machine learning algorithms (MLAs) that can self-learn a production process by comparing the results obtained with a defined threshold for electrical performance and/or defect size. This type of machine learning has already been used in a similar way for pass and fail cases [122]. More importantly, building a PE production database could enable continuous device performance improvement while reducing the costs associated with production. Finally, we believe that a closed-loop and ML-assisted analysis will enable the smart manufacturing of printed electronics, allowing it to emerge as a new large-scale and cost-effective technology.

### Data availability statement

No new data were created or analysed in this study.

### Acknowledgments

M Z expresses her gratitude to Mitacs Accelerate. F B gratefully acknowledges financial support from NSERC (2016-05020) and the Canada Research Chair tier 2 in THz technology (CRC-2019-127).

### ORCID iD

François Blanchard  <https://orcid.org/0000-0002-3335-7458>

### References

- [1] Gubbi J, Buyya R, Marusic S and Palaniswami M 2013 *Future Gener. Comput. Syst.* **29** 1645–60
- [2] Khan Y, Thielens A, Muin S, Ting J, Baumbauer C and Arias A C 2020 *Adv. Mater.* **32** 1905279
- [3] Bonnassieux Y et al 2021 *Flexible Printed Electron.* **6** 023001
- [4] Shirakawa H, Louis E J, MacDiarmid A G, Chiang C K and Heeger A J 1977 *J. Chem. Soc. Chem. Commun.* **16** 578–80
- [5] Keskinen M 2012 End-of-life options for printed electronics *Waste Electrical and Electronic Equipment (Weee) Handbook* (Amsterdam: Elsevier) pp 352–64
- [6] Bao Z, Feng Y, Dodabalapur A, Raju V and Lovinger A J 1997 *Chem. Mater.* **9** 1299–301
- [7] Khan S, Lorenzelli L and Dahiya R S 2014 *IEEE Sens. J.* **15** 3164–85
- [8] Trudeau C, Bolduc M, Beaupré P, Topart P, Alain C and Cloutier S 2017 *MRS Adv.* **2** 1015–20
- [9] Altay B N, Bolduc M and Cloutier S G 2020 Sustainable advanced manufacturing of printed electronics: An environmental consideration. *Green Energy and Environmen* **1**
- [10] Kamyshny A and Magdassi S 2014 *Small* **10** 3515–35
- [11] Bois C, Huppé M È, Rozel M and Trinh N D 2020 Printing techniques *Flexible, Wearable and Stretchable Electronics* (Boca Raton, FL: CRC Press) pp 107–36
- [12] Ermak O, Zenou M, Tokar G B, Ankri J, Shacham-Diamand Y and Kotler Z 2016 *Nanotechnology* **27** 385201
- [13] Kipphan H 2001 *Handbook of Print Media: Technologies and Production Methods* (Berlin: Springer Science & Business Media)
- [14] Ko S H, Pan H, Grigoropoulos C P, Luscombe C K, Fréchet J M and Poulidakos D 2007 *Nanotechnology* **18** 345202
- [15] Matsuhisa N, Kaltenbrunner M, Yokota T, Jinno H, Kuribara K, Sekitani T and Someya T 2015 *Nat. Commun.* **6** 7461
- [16] Mirka B, Fong D, Rice N A, Melville O A, Adronov A and Lessard B H 2019 *Chem. Mater.* **31** 2863–72
- [17] Selivanova M, Coady M J, Pignaneli J, Ocheje M U, Schlingman K, Malik A, Prado M and Rondeau-Gagne S 2020 *Flexible Printed Electron.* **5** 035001
- [18] Tousignant M N, Rice N A, Peltekoff A, Sundaresan C, Miao C, Hamad W Y and Lessard B H 2020 *Langmuir* **36** 3550–7
- [19] Tan H W, An J, Chua C K and Tran T 2019 *Adv. Electron. Mater.* **5** 1800831
- [20] Fukuda K and Someya T 2017 *Adv. Mater.* **29** 1602736
- [21] Trudeau C, Bolduc M, Beaupré P, Topart P, Alain C and Cloutier S 2017 *MRS Adv.* **2** 1015–20
- [22] Nguyen H A D, Lee J, Kim C H, Shin K H and Lee D 2013 *J. Micromech. Microeng.* **23** 095010
- [23] Mitra K Y, Kapadia S, Hartwig M, Sowade E, Xu Z, Baumann R R and Zichner R 2018 Process development of

- large area R2R printing and sintering of conductive patterns by inkjet and infra-red technologies tailored for printed electronics *Printing for Fabrication NIP Digit. Fabr. Conf. (Dresden, Germany, 23–27 September 2019)* (Society for Imaging Science and Technology) pp 21–32
- [24] Abbel R, Galagan Y and Groen P 2018 *Adv. Eng. Mater.* **20** 1701190
- [25] Khan S, Lorenzelli L and Dahiya R S 2014 *IEEE Sens. J.* **15** 3164–85
- [26] Rossander L H, Dam H F, Carlé J E, Helgesen M, Rajkovic I, Corazza M, Krebs F C and Andreassen J W 2017 *Energy Environ. Sci.* **10** 2411–19
- [27] Orrill M and LeBlanc S 2017 *J. Appl. Polym. Sci.* **134** 44256
- [28] Abu-Khalaf J et al 2018 *Sensors* **18** 3476
- [29] Diaz E, Ramon E and Carrabina J 2013 *Langmuir* **29** 12608–14
- [30] Beedasy V and Smith P J 2020 *Materials* **13** 704
- [31] Fajardo J, Garduño S I and Estrada M 2020 Analysis of inkjet printing conditions for ZnO nanoparticles patterns towards the fabrication of fully printed thin film devices 2020 *IEEE Latin America Electron Conf. (LAEDC)* (IEEE) pp 1–4
- [32] Mitra D, Mitra K Y, Dzhagan V, Pillai N, Zahn D R and Baumann R R 2018 *J. Electron. Mater.* **47** 2135–42
- [33] Perelaer J, Jani R, Grouchko M, Kamyshny A, Magdassi S and Schubert U S 2012 *Adv. Mater.* **24** 3993–8
- [34] Halonen E, Viiru T, Ostman K, Cabezas A L and Mantysalo M 2012 *IEEE Trans. Compon. Packag. Manuf. Technol.* **3** 350–6
- [35] Kamyshny A, Steinke J and Magdassi S 2011 Metal-based Inkjet Inks for Printed Electronics *Open Appl. Phys. J.* **4** 19–36
- [36] Eun K, Chon M W, Yoo T H, Song Y W and Choa S H 2015 *Microelectron. Reliab.* **55** 838–45
- [37] Sowade E, Polomoshnov M and Baumann R R 2016 *Org. Electron.* **37** 428–38
- [38] Perelaer J and Schubert U S 2013 *J. Mater. Res.* **28** 564–73
- [39] Bolduc M, Trudeau C, Beaupré P, Cloutier S and Galarneau P 2018 *Sci. Rep.* **8** 1418
- [40] Tone R and Ganz S 2016 Characterization techniques for printed electronics *Organic and Printed Electronics: Fundamentals and Applications* ed G Nisato, D Lupo and S Ganz (Boca Raton, FL: CRC Press) pp 117–47
- [41] Perelaer J, Smith P J, Mager D, Soltman D, Volkman S K, Subramanian V, Korvink J G and Schubert U S 2010 *J. Mater. Chem.* **20** 8446–53
- [42] Keikhaie M, Akbari J, Movahhedi M R and Alemohammad H 2014 Sintering characterizations of Ag-nano film on silicon substrate *4th International Conference on Ultrafine-Grained and Nano-structured Materials Advanced Materials Research (Tehran, Iran, 5–6 November 2013)* vol 829 (Trans Tech Publ) pp 342–6
- [43] Abbel R, van Lammeren T, Hendriks R, Ploegmakers J, Rubingh E J, Meinders E R and Groen W A 2012 *MRS Commun.* **2** 145–50
- [44] Rahman M S, Shahzadeh M, Rahman M, Pisana S and Grau G 2020 *Flex. Print. Electron.* **5** 035006
- [45] Jang Y R, Joo S J, Chu J H, Uhm H J, Park J W, Ryu C H, Yu M H and Kim H S 2021 *Int. J. Precis. Eng. Manuf.-Green Technol.* **8** 327–63
- [46] Hunt R W G and Pointer M R 2011 *Measuring Colour* (New York: Wiley)
- [47] Pipes A 2005 *Production for Graphic Designers* 4th edition (London: Laurence King Publishing) 166–67
- [48] Castrejón-García R, Castrejón-Pita J, Martín G and Hutchings I 2011 *Rev. Mex. Fis.* **57** 266–75
- [49] Strobel M, Jones V, Lyons C S, Ulsh M, Kushner M J, Dorai R and Branch M C 2003 *Plasmas Polym.* **8** 61–95
- [50] Logothetidis S, Georgiou D, Laskarakis A, Koidis C and Kalfagiannis N 2013 *Sol. Energy Mater. Sol. Cells* **112** 144–56
- [51] Cruz S M F, Rocha L A and Viana J C 2018 Printing technologies on flexible substrates for printed electronics *Flexible Electronics* (IntechOpen)
- [52] Hösel M, Dam H F and Krebs F C 2015 *Energy Technol.* **3** 293–304
- [53] Chen W, Nikiforov M P and Darling S B 2012 *Energy Environ. Sci.* **5** 8045–74
- [54] Saini R, Saini S and Sharma S 2010 *J. Cutaneous Aesthetic Surg.* **3** 32
- [55] Fu Q, Stein M, Li W, Zheng J and Kruis F E 2019 *Nanotechnology* **31** 025302
- [56] Greer J R and Street R A 2007 *J. Appl. Phys.* **101** 103529
- [57] Chung W H, Hwang H J, Lee S H and Kim H S 2012 *Nanotechnology* **24** 035202
- [58] Lee Y, Choi J R, Lee K J, Stott N E and Kim D 2008 *Nanotechnology* **19** 415604
- [59] Sneek A, Mäkelä T and Alastalo A 2018 *Flexible Printed Electron.* **3** 014001
- [60] Merilampi S, Björninen T, Haukka V, Ruuskanen P, Ukkonen L and Sydänheimo L 2010 *Microelectron. Reliab.* **50** 2001–11
- [61] He P, Cao J, Ding H, Liu C, Neilson J, Li Z, Kinloch I A and Derby B 2019 *ACS Appl. Mater. Interfaces* **11** 32225–34
- [62] Halonen E et al 2013
- [63] Lee D J, Oh J H and Bae H S 2010 *Mater. Lett.* **64** 1069–72
- [64] Fosso N, de Barros D P, Krähnenbühl J and Schintke S 2017 Printing and characterizing plasmonic nanoparticles 2017 *19th Int. Conf. on Transparent Optical Networks (ICTON)* (IEEE) pp 1–4
- [65] Dante M, Peet J and Nguyen T Q 2008 *J. Phys. Chem. C* **112** 7241–9
- [66] Greer J R and Street R A 2007 *Acta Mater.* **55** 6345–9
- [67] Kim S and Sung H J 2015 *J. Micromech. Microeng.* **25** 045004
- [68] Zhou X, Xu H, Cheng J, Zhao N and Chen S C 2015 *Sci. Rep.* **5** 1–10
- [69] Du X, Hardt D and Anthony B 2019 *IEEE Trans. Ind. Electron.* **67** 4077–87
- [70] Hedstrom S, Henriksson P, Wang E, Andersson M R and Persson P 2015 *J. Phys. Chem. C* **119** 6453–63
- [71] Pastorelli F, Accanto N, Jørgensen M, van Hulst N F and Krebs F C 2017 *Sci. Rep.* **7** 3787
- [72] Rösch R, Krebs F C, Tanenbaum D M and Hoppe H 2012 *Sol. Energy Mater. Sol. Cells* **97** 176–80
- [73] Rossander L H, Zawacka N K, Dam H F, Krebs F C and Andreassen J W 2014 *AIP Adv.* **4** 087105
- [74] West J, Carter M, Smith S and Sears J 2012 Photonic sintering of silver nanoparticles: comparison of experiment and theory *Sintering: Methods and Products* IntechOpen ed V Shatokha (Rijeka: InTech) pp 173–78
- [75] Gu W and Cui Z 2016 Photonic sintering of nano-silver conductive ink for printed electronics 2016 *6th Electronic System-Integration Conf. (ESTC)* (IEEE) pp 1–4
- [76] Dong Y, Lin Z, Li X, Zhu Q, Li J G and Sun X 2018 *J. Mater. Chem. C* **6** 6406–15
- [77] Zenou M, Ermak O, Saar A and Kotler Z 2013 *J. Phys. D: Appl. Phys.* **47** 025501
- [78] Cherrington M, Claypole T, Gethin D, Worsley D and Deganello D 2012 *Thin Solid Films* **522** 412–14
- [79] Wijdekop M, Arnold J, Evans M, John V and Lloyd A 2005 *Mater. Sci. Technol.* **21** 791–7
- [80] Lee K J, Jun B H, Kim T H and Joung J 2006 *Nanotechnology* **17** 2424
- [81] Grubb P M, Mokhtari Koushyar F, Lenz T, Asghari A, Gan G, Xia W, Dalir H, Subbaraman H and Chen R T 2019 *J. Manuf. Mater. Process.* **3** 33
- [82] Hoath S D 2016 *Fundamentals of Inkjet Printing: The Science of Inkjet and Droplets* (New York: Wiley)
- [83] Zhuldybina M, Ropagnol X, Bois C, Zednik R J and Blanchard F 2020 *npj Flexible Electron.* **4** 21
- [84] Panin A, Shugurov A and Oskomov K 2005 *Phys. Solid State* **47** 2055–9

- [85] Huemer F, Jamalieh M, Bammer F and Hönig D 2016 *tm-Tech. Mess.* **83** 549–56
- [86] Janesch J 2013 Two-wire versus four-wire resistance measurements: which configuration makes sense for your application? *Technical Report Keithley Instruments* 2–4
- [87] Chen W, Nikiforov M P and Darling S B 2012 *Energy Environ. Sci.* **5** 8045–74
- [88] de la Fuente Vornbrock A, Ding J M, Sung D, Tseng H Y and Subramanian V 2009 Printing and scaling of metallic traces and capacitors using a laboratory-scale rotogravure press 2009 *Flexible Electronics & Conf. and Exhibition* (IEEE) pp 1–7
- [89] Seifert T, Sowade E, Roscher F, Wiemer M, Gessner T and Baumann R R 2015 *Ind. Eng. Chem. Res.* **54** 769–79
- [90] Zabihi F, Xie Y, Gao S and Eslamian M 2015 *Appl. Surf. Sci.* **338** 163–77
- [91] Duparre A, Ferre-Borrull J, Glied S, Notni G, Steinert J and Bennett J M 2002 *Appl. Opt.* **41** 154–71
- [92] Madsen M H and Hansen P E 2016 *Surf. Topography: Metrol. Prop.* **4** 023003
- [93] Seong J, Kim S, Park J, Lee D and Shin K H 2015 *Int. J. Precis. Eng. Manuf.* **16** 2265–70
- [94] Yilmaz S 2015 *J. Semicond.* **36** 082001
- [95] Hwang H J, Chung W H and Kim H S 2012 *Nanotechnology* **23** 485205
- [96] Feng X, Su R, Happonen T, Liu J and Leach R 2018 *Opt. Express* **26** 13927–37
- [97] Shimanovich K, Bouhadana Y, Keller D A, Rühle S, Anderson A Y and Zaban A 2014 *Rev. Sci. Instrum.* **85** 055103
- [98] Kolassa N, Punzengruber C, Suko J and Makinose M 1979 *FEBS Lett.* **108** 495–500
- [99] Dam H F et al 2015 *Adv. Energy Mater.* **5** 1400736
- [100] Pröller S, Liu F, Zhu C, Wang C, Russell T P, Hexemer A, Müller-Buschbaum P and Herzog E M 2016 *Adv. Energy Mater.* **6** 1501580
- [101] Rossander L H, Zawacka N K, Dam H F, Krebs F C and Andreasen J W 2014 *AIP Adv.* **4** 087105
- [102] Espinosa N et al 2013 *J. Mater. Chem. A* **1** 7037–49
- [103] Garcia-Martin J, Gomez-Gil J and Vazquez-Sanchez E 2011 *Sensors* **11** 2525–65
- [104] Lewis A P, Hunt C, Thomas O and Wickham M 2017 *Flexible Printed Electron.* **2** 044001
- [105] Remes K, Latomäki A and Fabritius T 2019 Flexible electronics non-destructive uniformity characterization by synchronized thermography 2019 *IEEE Int. Instrumentation and Measurement Conf. (I2MTC)* (IEEE) pp 1–5
- [106] Remes K, Järvenpää A and Fabritius T 2019 *Opt. Lett.* **44** 2574–7
- [107] Remes K and Fabritius T 2019 *IEEE Trans. Instrum. Meas.* **69** 2390–7
- [108] Tao Y H, Fitzgerald A J and Wallace V P 2020 *Sensors* **20** 712
- [109] Chen X and Pickwell-MacPherson E 2019 *Sensors* **19** 4118
- [110] Naftaly M, Vieweg N and Deninger A 2019 *Sensors* **19** 4203
- [111] Zhong S 2019 *Frontiers Mech. Eng.* **14** 273–81
- [112] Gowen A A, O’Sullivan C and O’Donnell C 2012 *Trends Food Sci. Technol.* **25** 40–6
- [113] Jansen C et al 2010 *Appl. Opt.* **49** E48–57
- [114] Zhuldybina M, Ropagnon X, Trudeau C, Bolduc M, Zednik R J and Blanchard F 2019 *Sensors* **19** 444
- [115] Neu J and Schmuttenmaer C A 2018 *J. Appl. Phys.* **124** 231101
- [116] Redo-Sanchez A, Laman N, Schulkin B and Tongue T 2013 *J. Infrared Millim. Terahertz Waves* **34** 500–18
- [117] Zhang J, Tang J, Sun W, Zhang Y, Wang X and Yang B 2019 *Electronics* **8** 674
- [118] Zeng Y, Edwards M, Stevens R, Bowen J W, Donnan R S and Yang B 2017 *Org. Electron.* **48** 382–8
- [119] Blanchard F, Doi A, Tanaka T, Hirori H, Tanaka H, Kadoya Y and Tanaka K 2011 *Opt. Express* **19** 8277–84
- [120] Blanchard F, Doi A, Tanaka T and Tanaka K 2013 *Ann. Rev. Mater. Res.* **43** 237–59
- [121] Guiramand L, Zhuldybina M, Arikawa T, Tanaka K and Blanchard F 2020 Near-field thz imaging of a printed metallic checkerboard pattern *Nonlinear Photonics (Optical Society of America) (Montreal, Canada, 13–16 July 2020)* NpTu4D-16
- [122] Oberai A and Kamoji R 2020 *Microelectron. Reliab.* **114** 113822